Experimental and Theoretical Design of Advanced High-Entropy Alloys and Application in Al-Fe Dissimilar Welding

A Dissertation Presented for the
Doctor of Philosophy
Degree
The University of Tennessee, Knoxville

Peiyong Chen
December 2021

ACKNOWLEDGEMENTS

I am grateful for whoever helped me in during my PhD journey. First of all, I would like to thank my parents, Xieyi Chen and Shaorong Cen, and my sister, Yuting Chen. Without their support, I cannot get to this step.

I would like to thank my advisor, Dr. Peter. K. Liaw. He is a very hard-working person and set me a very outstanding example on how to succeed on my own career. I would like to grant my gratitude to my other committee members, Dr. Kurt E. Sickafus, Dr. Yanfei Gao, and Dr. Hairong Qi. I would like to thank Dr. Jim Hu, who is the project manager from Honda R&D. He guides me a lot and show me what research we can do in the industry field. I would like to thank Dr. Carl Lundin, who was an expert on welding field. He contributes a lot on the success of the project and give me a lot of suggestions to think about the research. I would like to thank Dr. David Keffer for his teaching on the molecular dynamics class. I admire his true passion on research and from hi I really learn a lot.

My thanks also go to Ms. Carla Lawrence, Ms. Gena Jenkins, Ms. Martha Gale, Ms. Tonya Brewer, Ms. Tracy Lee, Mr. Frank Holiway, Mr. Randy Stooksbury, Mr. Stephen Stiner, Mr. Adam Cain, Ms. Ms. Ashledy Cole, Ms. Tonya Goins, and Ms. Tracy Mandrekas in our department for their great help.

I would like to thank all of my student colleagues for their help and friendship. I am especially grateful to Dr. Xie Xie, Dr. Haoling Jia, Dr. Zhiqian Sun, Dr. Zhi Tang, Dr. Bilin Chen, Dr. Tong Yang, Dr. Lu Huang, Dr. Gian Song, Dr. Louis J. Santodonato, Dr. Haoyan Diao, Dr. Shuying Chen, Dr. Rui Feng, Dr. Shaoyu Wang, Dr. Chanho Lee, Mr. Xuesong

Fan, Mr. Zongyang Lyu, Ms. Di Xie, Dr. Yangyang Zhao, Dr. Yuan Li, Dr. Peijun Hou, and Dr. Jamieson Brechtl at UT. I also thank many visiting scholars in our group.

I would like to acknowledge the financial support from the Honda R&D and U.S. Army Research Office under project number of W911NF-13-1-0438.

ABSTRACT

Weight reduction is always an important topic in the automobile industry, for energy and natural resource savings. To achieve this goal, a lot of studies have been conducted on the dissimilar welding to join aluminum with steel. In the present work, a novel idea is come up to apply high-entropy alloys as interlayers into the dissimilar welding between aluminum and steel. In the past decades, high-entropy alloys (HEAs) have drawn great attention due to their unique single-phase microstructures and outstanding mechanical properties as structural materials. In this work, three tasks are come up for the investigation: using current HEAs on the dissimilar welding, design HEAs with desired properties based on the prior work, and conduct welding study and analysis on dissimilar welding with designed HEAs.

In the first task, the Al0.1CoCrFeNi and Al0.3CoCrFeNi HEAs are selected to be the interlayers. The insights obtained in this study offer an understanding of how the current face-centered cubic (FCC) HEAs will work on dissimilar welding. In the second task, due to the problems that exist in the first task, new HEAs that fit with the dissimilar welding need to be developed. In order to fulfill this task and find out the best HEAs for trial, a technique, high

throughput calculation (HTC) which is based on calculations of phase diagrams (CALPHADs), is applied for the search of the vast compositional space of HEAs. New HEAs with desired properties are designed, fabricated, and characterized. In the third task, a welding study is conducted with the designed HEAs. Solidification analysis with CALPHAD is conducted, based on the model came up by Dr. Sindo Kou. A criterion for solidification cracking is applied to evaluate the susceptibility. The present work shows that with newly designed HEAs by the second task, a fusion zone with the mixing of the aluminum alloys, steel, and HEAs is obtained for the first time. New HEA compositions are proposed for future work.

TABLE OF CONTENTS

LIST OF TABLES

LIST OF FIGURES

CHAPTER ONE
INTRODUCTION

1.1 Objective and motivation

The goal of this proposal is to (1) provide an understanding of Al0. high-entropy alloys (HEAs) serving as intermedia materials in resistance spot welding (RSW) between selected aluminum alloys and steels; (2) based on the fundamental study of welding results obtained from the present work, design and develop HEAs that are more suitable in the Al – steels dissimilar welding coupled with experiments and simulation methods. The proposed work will take advantage of the integration of alloys design and processing, mechanical testing, microstructural characterization, and simulation modeling.

Welding is a basic and important fabrication process in industry. There are many welding methods, such as shield - metal - arc welding, gas welding, laser - beam welding, electron - beam welding, resistance - spot welding, etc. Among these welding methods, resistance - spot welding is one of the most important welding methods in the auto industry. In the automobile industry, to assemble a car body, 7,000 to 12,000 spots of welding are needed according to the size of the car [1]. In the resistance - spot welding, the overlapping sheets are positioned between the electrodes with a water - cooling condition, and then are heated by a large electronic current within a short time. Besides, resistance - spot welding can be completely automated with industrial robots on assembly lines, which is beneficial to the productivity and cost. With the relatively - mature resistance - spot welding technique, the cost of auto fabrication is greatly decreased. An important topic in the automobile industry

is weight reduction, for energy and nature resource savings. Among the light - weight materials, aluminum alloys are attractive structural alloys for the weight reduction in the automobile body. However, considering strength, cost, and joining processing, multi - material structures are in practice. Taking the material supply into account, aluminum alloys and steels are the most promising materials for the automobile. However, welding aluminum alloys to steels is always a great challenge even up to now due to the reasons that: large electrochemical difference of 1.22 volts; different thermal properties; dissimilar thermal expansion; different heat capacity and thermal conductivity; large difference of the melting points (around 660 °C for Al alloys and around 1500 °C for steels); and nearly zero solid solubility of iron in aluminum. These lead to distortion, formation of cracks and porosity, and formation of brittle intermetallics after the welding process. An idea is come up by this proposal to apply HEAs as an interlayer in the RSW between Al alloys and steels.

The proposed work will integrate (1) the HEAs alloy design and processing, (2) welding experiments and mechanical tests, (3) microstructural characterizations, and (4) calculation of phase diagrams (CALPHADs). The results are expected to offer an initial understanding of applying HEAs into RSW between selected Al alloys and steels, and encourage the development of advanced HEAs. Above all, the proposed study could offer a new approach to solve the challenge of dissimilar welding between Al alloys and steels with HEAs, and contribute to the development of novel and advanced HEAs.

1.2 Hypothesis

The author of this proposal hypothesizes that suitable HEAs could be served in the RSW as an interlayer between Al alloys and steels due to the reasons that: (1) the concept of HEAs with single phase and high mixing of configurational entropy could avoid the formation of brittle intermetallics; (2) good self - weldability of some single phase HEAs as reported in the previous studies; (3) with superior corrosion and fatigue properties, HEAs have great potential to serve as a welding joint in the aspect of mechanical property. A schematic to explain how the welding for these three materials are shown in Figure 1.1.

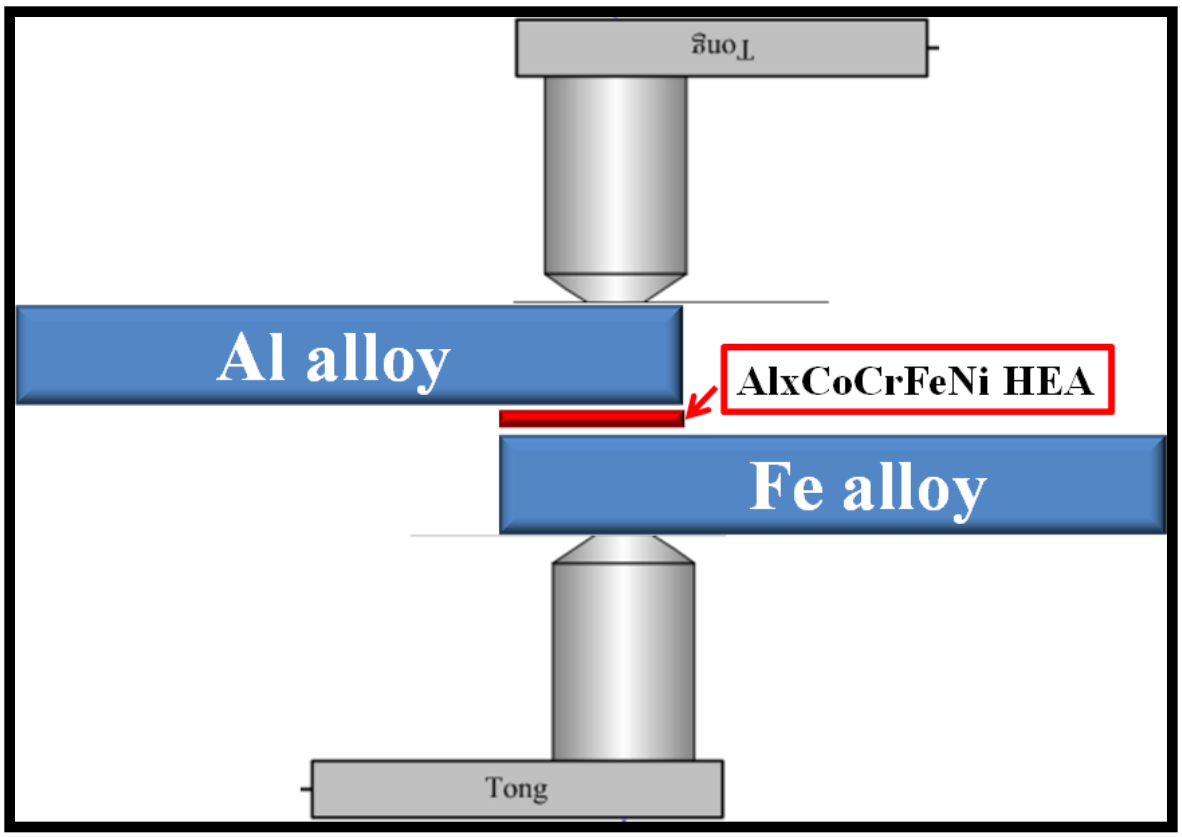

Figure 1.1. Schematic of applying HEAs into RSW between Al alloys and steels.

CHAPTER TWO
LITERATURE REVIEW

2.1 High Entropy alloys

Great research attention has been drawn to HEAs in recent time. Unlike conventional alloys, which are based on one or two principal elements, HEAs are defined as alloys that are composed of five or more elements, with atomic concentrations of each element varying from 5 to 35 at.% [2]. The purpose of this alloy design is to maximize the configurational entropy, ΔS_{conf}, to suppress the formation of intermetallics or order phases and easily obtain solid-solution phases, such as face-center-cubic (FCC), body-center-cubic (BCC), and hexagonal-close-packed (HCP) structures [3-13]. Recent studies have revealed that HEAs have superior properties, such as high yield strength, high strength at elevated temperatures, excellent corrosion resistance, and good fatigue properties [2-6, 10, 14-18].

2.2 CALPHAD

The CALPHAD approach, which primarily aims at calculating phase equilibria and thermodynamic properties of complex multi-component, multi-phase systems, emerged in the late 1950s and became an active research field since the 1970s [19, 20]. The essence of the CALPHAD approach is to obtain self-consistent thermodynamic descriptions of the lower order systems: binaries and ternaries, in terms of known thermodynamic properties and phase equilibrium data. A thermodynamic description (or usually called thermodynamic database) compiles the Gibbs energy functions of a system being studied. The advantage of this method is that the separately measured phase diagrams and

thermodynamic properties can be represented by the same thermodynamic description of a materials system in question. More importantly, a multi-component thermodynamic database can be built up through those of the constituent lower order systems using geometric models, and such a database enables us to calculate phase diagrams of the multi-component systems that are experimentally unavailable.

The primary task of phase-diagram calculations is therefore to build a thermodynamic database, i.e., to develop the Gibbs energy functions of all the phases in the system to be studied. According to the physical nature of the phases in the metallic alloys, they are usually categorized as: disordered solution phases, ordered intermetallic phases, and stoichiometric compounds (or called line compounds). The thermodynamic models to be used to describe these three types of phases are presented below. The equations are given for a binary system, and they can be extrapolated to a multi-component system using geometric models, such as Muggianu model [21].

The Gibbs energy of a binary solution phase can be written as:

$$G_m^{\varphi} = \sum_{i=A,B} x_i \cdot G_i^{\varphi,o} + RT \sum_{i=A,B} x_i \ln x_i + x_A \cdot x_B \sum_{v} L_v \cdot (x_A - x_B)^v \qquad (1)$$

where the first term on the right hand of the equation represents the reference states with x_i, the mole fraction of a component, *i*, and $G_i^{\varphi,o}$, the Gibbs energy of a pure component, *i*, with an φ structure; the second term is the ideal mixing term with R, the gas constant, and T, the temperature; the last term is the excess Gibbs energy of mixing with L_v, the interaction coefficient, and ν, the power of the polynomial series. When ν = 0, it is a regular solution model, and when ν = 0 and 1, it is a sub-regular solution model, and so on. The liquid phase and disordered solid-solution phases can be described by this model.

An ordered intermetallic phase is described by a variety of sublattice models, such as the compound-energy formalism [22]. In these models, the Gibbs energy is a function of the sublattice species concentrations and temperature. The Gibbs energy of a binary intermetallic phase, described by a two-sublattice compound-energy formalism, $(A,B)_p:(A,B)_q$, can be written as:

$$\begin{aligned} G_m^{\varphi} = & \sum_{i=A,B}\sum_{j=A,B} y_i^I y_j^{II} G_{i:j}^{\varphi} + RT[\frac{p}{p+q}\sum_{i=A,B} y_i^I \ln y_i^I + \frac{q}{p+q}\sum_{i=A,B} y_i^{II} \ln y_i^{II}] \\ & + \sum_{j=A,B} y_A^I y_B^I y_j^{II} \sum_{v} (y_A^I - y_B^I)^v L_{A,B:j}^v + \sum_{i=A,B} y_i^I y_A^{II} y_B^{II} \sum_{v} (y_A^{II} - y_B^{II})^v L_{i:A,B}^v \\ & + y_A^I y_B^I y_A^{II} y_B^{II} L_{A,B:A,B} \end{aligned} \tag{2}$$

where y_i^I and y_i^{II} are the species concentrations of a component, *i*, in the first and second sublattices, respectively. The first term on the right hand of the equation represents the reference state with the mechanical mixture of the stable or hypothetical compounds: A, A_pB_q, B_pA_q, and B. $G_{i:j}^{\varphi}$ is the Gibbs energy of the stoichiometric compound, $i_p j_q$, with an φ structure. The value of $G_{i:j}^{\varphi}$ can be obtained experimentally, if $i_p j_q$ is a stable compound. For a hypothetical compound, its Gibbs energy can be obtained by ab initio calculations. The second term is the ideal mixing Gibbs energy, which corresponds to the random mixing of species on each sublattice. The last three terms are the excess Gibbs energies of mixing. The "*L*" parameters in these terms are model parameters whose values are optimized, using the experimental phase-equilibrium data and thermodynamic-property data. These parameters can be temperature dependent. Intermetallic phases, such as B2 phase, can be described by the compound-energy formalism.

The Gibbs energy of a binary stoichiometric compound, A_pB_q, G_m^{φ}, is described only as a function of temperature:

$$G_m^{\varphi} = \sum_i x_i G_i^{\varphi,\circ} + \Delta_f G(A_pB_q) \tag{3}$$

where x_i is the mole fraction of component, *i*, and $G_i^{\varphi,\circ}$ represents the Gibbs energy of component, *i* with an φ structure; $\Delta_f G(A_pB_q)$, which is normally a function of temperature, represents the Gibbs energy of formation of the stoichiometric compound. If $\Delta_f G(A_pB_q)$ is a linear function of temperature:

$$\Delta_f G(A_pB_q) = \Delta_f H(A_pB_q) - T \cdot \Delta_f S(A_pB_q) \tag{4}$$

then $\Delta_f H(A_pB_q)$ and $\Delta_f S(A_pB_q)$ are the enthalpy and entropy of formation of the stoichiometric compound, respectively.

The procedure of developing a thermodynamic description for a binary system are: (i) determine the phases in the system, (ii) select a proper thermodynamic model for each phase, (iii) collect the available experimental and theoretical data on the system, and (iv) optimize the model parameters for each phase. The Gibbs-energy functions thus obtained can be used to calculate the phase stability for the binary system. The strategy of building a multi-component thermodynamic database starts with deriving the thermodynamic description of every constituent binary in the system. There are C_n^2 constituent binaries in an n-component alloy system, where

$$C_n^i = \frac{n!}{i!(n-i)!} \tag{5}$$

To develop a reliable database, the Gibbs energies of these binaries must be developed in a self-consistent manner and be compatible with each other. Three binaries form a ternary, and a preliminary thermodynamic description can be obtained by combining the three constituent binaries using geometric models, such as the Muggianu model [21]. In some cases, a ternary database developed in this way can describe a ternary system fairly well, while in most cases, ternary interaction parameters are necessary to better describe the ternary system. If a new phase appears in the ternary, which is not in any of the constituent binaries, a thermodynamic model is selected for this ternary phase, and its model parameters are optimized, using the experimental information for this ternary phase. There are a total of C_n^3 ternary systems in an n-component system. After thermodynamic descriptions of all the ternaries are established, the model parameters are simply used to describe quaternary and higher-order systems using an extrapolation approach. High-order interaction parameters are usually not necessary because although interactions between binary components are strong, in ternary systems they become weaker, and in higher-ordered systems they become negligibly weak [23, 24].

2.3 Current research on HEA welding

The research of HEAs which are related to welding techniques, are ongoing in recent years [25-33]. Xing-Wu et al. prepared the Al2CrFeCoCuTiNix by laser cladding on substrate Q235 steel, then investigated the microstructure and properties [25]. They found a good combination of the bounding between HEAs cladding layer and the substrate steel, together with that the surface cladding layer has higher hardness and good corrosion resistance [25].

Victor et al. uses AlCoCrFeNi as a filler metal and deposit it on a steel support by tungsten inner gas (TIG) welding process [26]. They found the AlCoCrFeNi HEA has higher hardness than the base carbon steels [26]. Komarasamy et al. applied friction stir – processing (FSP) on the Al0.1CoCrFeNi HEA and studied the microstructure [27]. Grain refinement from several millimeters in as-received condition to 0.35 – 15 micrometers after FSP is found [27]. An extensive increase of the yield strength is observed after grain refinement [27].

In 2015, Wu et al. from ORNL research group investigated the weldability of the single FCC phase CrMnFeCoNi HEA by electron beam welding [28]. They found the grain structure of the fusion zone (FZ) is controlled by the solidification behavior of the welding pool, together with no formation of cracking in the FZ [28]. Figure 2.1 shows the (a) grain structure with annealing twins of the initial CrMnFeCoNi HEA; (b-e) shows that neither solidification cracking nor cracks in or near the heat affected zone (HAZ) were observed from the top surface and the transverse surface of the samples after welding; (f) EDS mapping shows uniform elemental distribution is still maintained after welding in the whole samples [28]. The no cracking behavior is attributed to the narrow freezing range (~ 60°C) of the CrMnFeCoNi HEA and large high temperature solid solution between most pairs of two elements (for example, complete solid solution between Ni and Co) [28]. The welded materials maintained the strength and ductility of the base materials (BM) at both room and cryogenic temperatures, which indicated good weldability in this condition [28].

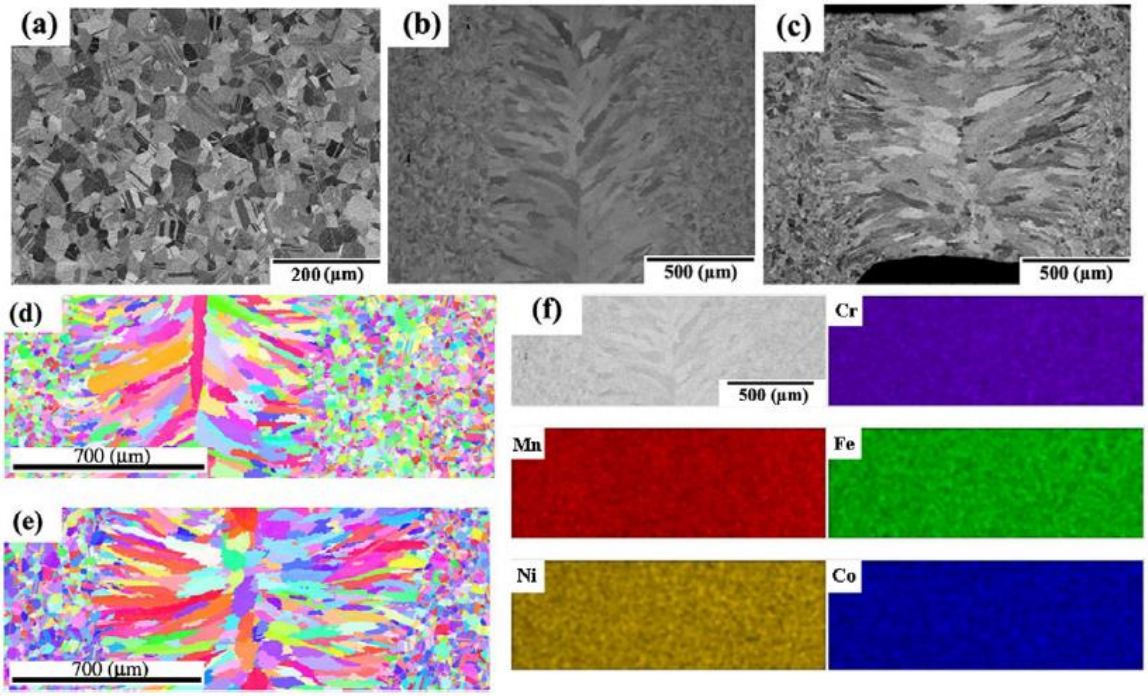

Figure 2.1. Backscattered electron images of (a) the initial alloys, (b) the top surface, and (c) the transverse surface of the weld. (d, e) EBSD images of the top surface and the transverse surface of the weld, respectively. (f) Elemental distribution around the weld [28].

In 2017, Zhu et al. reported a study on friction stir welding of the as-cast Al0.3CoCrFeNi HEA [29]. Figure 2.2 (a) and (b) show the crossing section of the welded samples with the welding speed of 50 and 30 mm/min, respectively; (c-g) illustrate the microstructure of the different four region, BM, HAZ, thermomechanically affected zone (TMAZ) and stir zone (SZ), of the samples, which shows that grain refinement structure, no phase transformation and no precipitate in the SZ [29]. The SZ shows the highest hardness, which corresponds to the microstructure [29].

In 2018, Sokkalingam et al. reported an investigation on using the laser beam welding technique on the as – cast Al0.5CoCrFeNi HEA [32]. The microstructure of the as-welded samples shows a typical FZ microstructure with dendritic structure with a reduction in BCC phase due to the minimal segregation of the ratio at the interdendrites, which corresponds to the reduction in the hardness of the FZ, comparing to the BM [32].

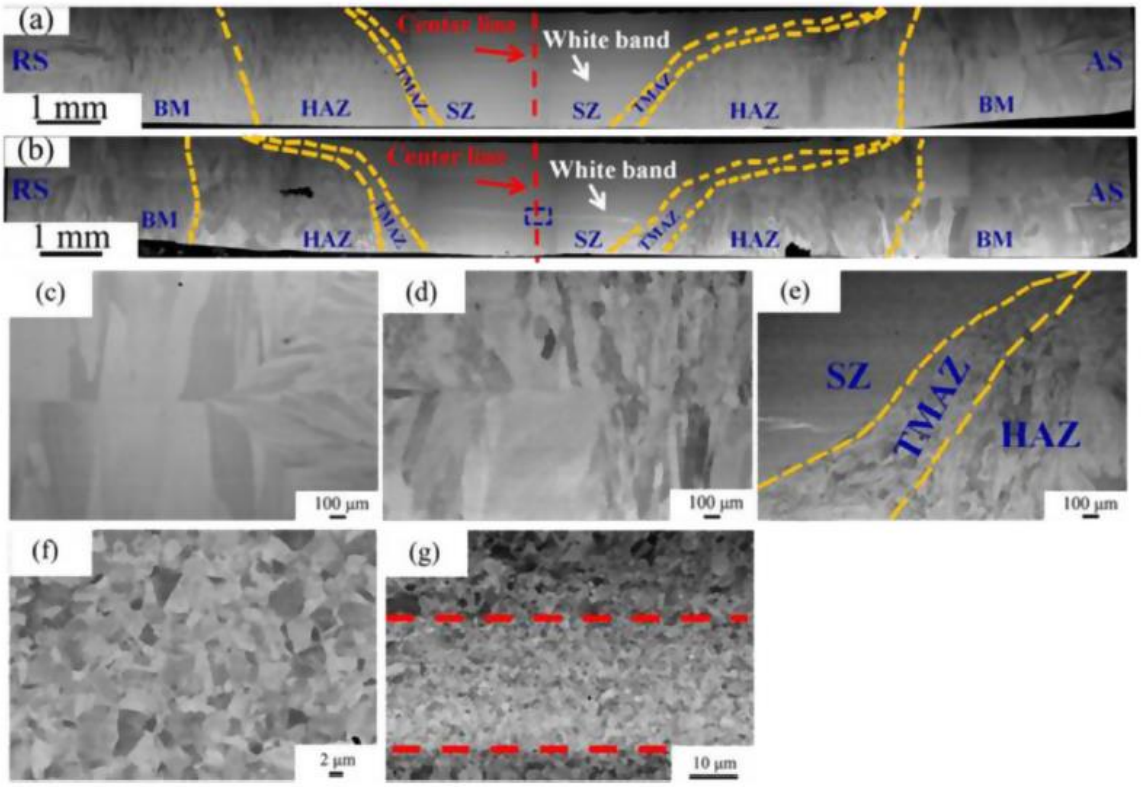

Figure 2.2. Macrostructure of the cross section of FSWed joints with speed of (a) 50 mm/min and (b) 30 mm/min. (c–f) Correspond to the microstructure of the BM, HAZ, TMAZ, and SZ, respectively with speed of 30 mm/min. (g) Shows the enlarged microstructure of the marked rectangular region in the (b) [29].

CHAPTER THREE
STUDY ON FE-AL DISSIMILAR WELDING WITH AL0.3COCRFENI HEAS INTERLAYERS

3.1 Introduction

To reduce fuel consumption and enhance fuel efficiency, aerospace and automotive industries have put great attention on weight reduction of component. Considering the aspects of performance, cost, and weight, introducing aluminum alloys to steels body are one of the most attractive alloy combinations to reduce weight in machine bodies. Owing to efficiency and volume of production, resistance spot welding (RSW) is one of the most important joining methods in automotive industries. To produce the hybrid structure of Aluminum alloys and steels, a technology to make dissimilar Al/Fe joints is needed, especially with RSW since it is very commonly used in the industries. However, due to the great intrinsic difference in thermal, electrical and mechanical properties, brittle intermetallic compounds are always formed in the welding joint between aluminum alloys and steels which will lead to degradation of mechanical properties [34-42]. Shanglu et al. investigated the welding of the aluminum alloy, 6061 - T6 [Al - 0.04Cr - 0.3Cu - 0.7Fe - 1.0Mg - 0.15Mn - 0.6Si - 0.15Ti - 0.25Zn, weight percent (wt.%)], to zinc - coated steel (0.05 to 0.25% carbon content) by the cold - metal - transfer method [41]. Cracking and lack of fusion between steels and aluminum alloys are observed. Torkamany et al. studied the welding of the carbon steel (Fe - 0.4Mn - 0.04C wt.%) to 5754 aluminum alloy (Al - 0.12Si - 0.04Cu - 0.25Mn - 3.009Mg - 0.08Cr - 0.006Ni - 0.37Fe wt.%) by Nd with laser

welding [39]. Pores and pre-crack are found, along with the Fe - Al intermetallics. Ranfeng et al. reported the resistance - spot welding on the aluminum alloy, A5052 (Al - 2.2Mg - 0.27Fe - 0.19Cr - 0.09Si - 0.049Mn - 0.027Cu - 0.005Zn wt.%), to steel SPCC (Fe - 18Cr - 0.85Si - 1.25Mn - 0.06C - 0.04P - 0.02S wt.%), and austenitic - stainless steel SUS304 (Fe - 18.0Cr - 0.85Si - 1.25Mn - 0.06C - 0.04P - 0.02S - 8.0S wt.%) [36]. After the tensile tests, the strength of aluminum self - weld joint, A5052/A5052, is higher than the joints of A5052/SPCC and A5052/SUS304, which indicates that the joints between aluminum alloys and steels are not favorable. Satonaka et al. developed a new method termed the resistance - spot welding with a cover plate between the aluminum and electrode, to obtain higher temperature in the weld [43]. Ranfeng et al. then used this method to weld the aluminum A5052 to steel SPCC and steel SUS304 and obtain joints between the aluminum and steels with higher strength [35]. However, a large amount of Fe - Al intermetallics are still formed, which greatly affect the mechanical property of the joints.

3.2 Materials and Methods

3.2.1 Materials

The materials used in this investigation were JAC980 high-strength low-alloy steel with 1.0 mm thickness, 5754 aluminum alloys with 2.0 mm thickness, and $Al_{0.3}$CoCrFeNi HEA with 0.25 mm thickness. The chemical compositions of the steel and 5754 aluminum alloys are given in Table 3.1.

Table 3.1. Chemical composition of JAC 980 steel and 5754 aluminum alloy (by wt. %).

Materials	Si	C	Mn	P	S	Al	Mo	Ti	V	Cr	Fe
JAC 980YL (USS)	0.012	0.11	2.32	0.012	0.005	0.05	0.36	0.001	0.001	0.23	Bal
Al 5754	<0.40	/	<0.50	/	/	Bal	/	<0.15	/	<0.30	<0.40

3.2.2 Experimental details

The $Al_{0.3}$CoCrFeNi HEA is firstly casted into an ingot (2''×6''×15''). Then the ingot was hot rolled to plates of 0.125 inch thickness. After hot rolling, the plate was then cold rolled to foils of 0.25 mm and 0.5 mm thickness. The cold-rolled HEA foils were then subjected to a homogenization treatment at 1,200 °C for 3 hours and water quenched. The HEA foils were prepared with up to 1200 grits to remove surface oxidation and cleaned by acetone. Before welding, the steel and aluminum sheets were prepared by grade 400 SiC abrasive paper polishing and degreased with acetone. The joint configuration of these three materials is shown in Figure 3.1.

After welding, samples for microstructural characterization were prepared by cross-sectioning the center of the welding nugget which is perpendicular to the samples' surface plane. The samples were then ground, polished up to 1200 grit SiC paper. The morphology of the welding joint was examined by the optical microscope. The microstructure and chemical composition of the samples were characterized by the scanning electron microscopy (SEM) with the energy-dispersive spectroscopy (EDS).

Nano-indentation hardness tests were performed at room temperature using a Keysight Technologies G200 Nano-indenter with a Berkovich diamond (3-sided pyramidal tip) in continuous stiffness measurement mode with a constant loading rate of 400 μNs^{-1}. The depth dependent hardness and elastic modulus were calculated using the Oliver and Pharr method. Approximately 15-20 indents were taken per sample to ensure a proper statistical analysis of the data. Specimens were indented to a maximum depth of 800 nm in which the data below 100 nm was discarded due to high scatter caused by surface defects.

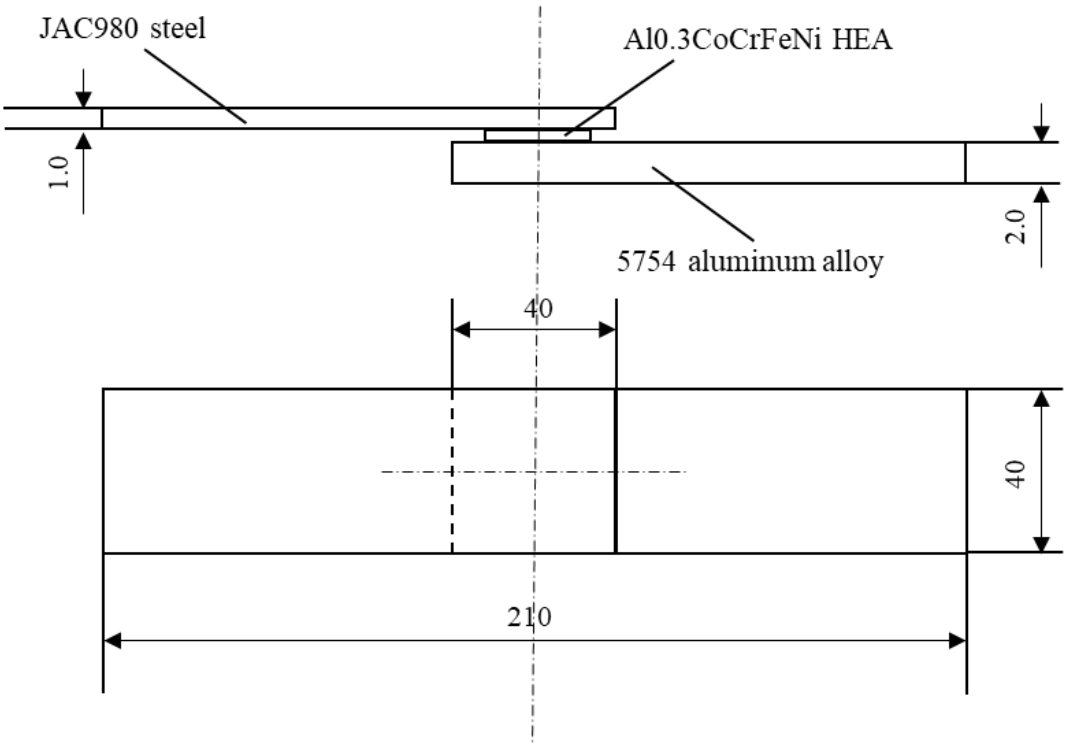

Figure 3.1. Geometry and dimensions of specimens for welding (not to scale, dimensions in mm)

3.2.3 Nano-indentation

Nano-indentation hardness tests were performed at room temperature using a Keysight Technologies G200 Nano-indenter with a Berkovich diamond (3-sided pyramidal tip) in continuous stiffness measurement mode with a constant loading rate of 400 μNs^{-1}. The depth dependent hardness and elastic modulus were calculated using the Oliver and Pharr method [44, 45]. Approximately 15-20 indents were taken per sample to ensure a proper statistical analysis of the data. Specimens were indented to a maximum depth of 800 nm in which the data below 100 nm was discarded due to high scatter caused by surface defects in the sample.

To examine the indentation size effect (ISE) [46] of the alloys, the hardness was plotted according to the following equation:

$$H = H_0 \sqrt{1 + \frac{h^*}{h}} \tag{6}$$

where H is the nanoindentation hardness, H_0 is the hardness associated with either the statistically stored dislocations, h is the indentation depth, and h^* are terms which characterize the depth dependence of the hardness.

$$h^* = \frac{81}{2} b\alpha^2 \tan^2\theta \left(\frac{\mu}{H_0}\right) \tag{7}$$

θ is the angle between the sample surface and the surface of the indenter (assumed to be conical θ is taken to be 19.7 ^{o} [47]), b is the Burgers vector, α is a geometric constant equal to 0.5 [46], and μ is the shear modulus.

3.3 Results and discussions

3.3.1 Joint microstructure

Figure 3.2 shows the welding joint between 5754 aluminum alloy, HEA, and JAC980. Pores and cracking are observed. Clear welding nugget is formed between JAC980 steel and the HEA.

3.3.2 Joint properties

To evaluate the mechanical properties of interfacial intermetallic compound layers, a nanoindentation test was performed, and the nanoindentation positions are shown in Figure 3.3. From the top to the bottom in Figure 3.3, it is 1) Al side 100 micro away from the interface Al/HEA; 2) Al side 50 micro away from the interface Al/HEA; 3) interdendrite layer; 4) HEA; 5) steel side away the interface steel/HEA; 6) steel side away from the interface steel /HEA.

Figure 3.4 shows the mean hardness of different spot as the indentation depth changes. As the indentation depth increases, the hardness of Al stays around 1.5 GPa. While Al0.3CoCrFeNi HEA has similar hardness with the interdendrites. Steel has the highest hardness. To negate the surface effect of nano-indentation, Nix-Gao Extrapolation is applied to obtain the bulk hardness. Figure 3.5 (a) shows the extrapolation of different spot. From Figure 3.5 (b) we can see that, after removing the surface effect, the hardness of the interdendrite (~3.5 GPa) is clearly higher than the HEA (~2 GPa) and the 5754 Al (~1.3 GPa). This strongly suggest that the interdendrite layer could be intermetallics which cause higher hardness.

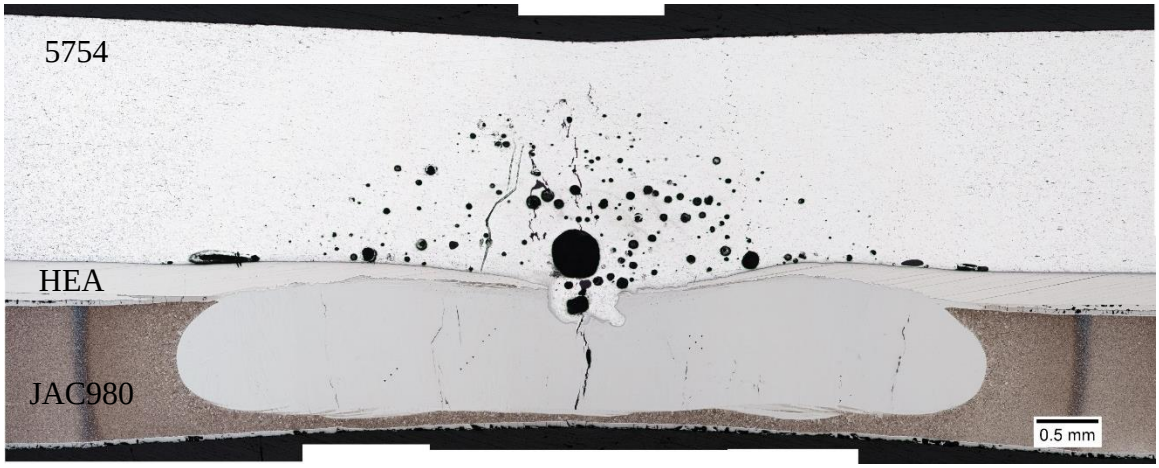

Figure 3.2. Optical image of the welding joint.

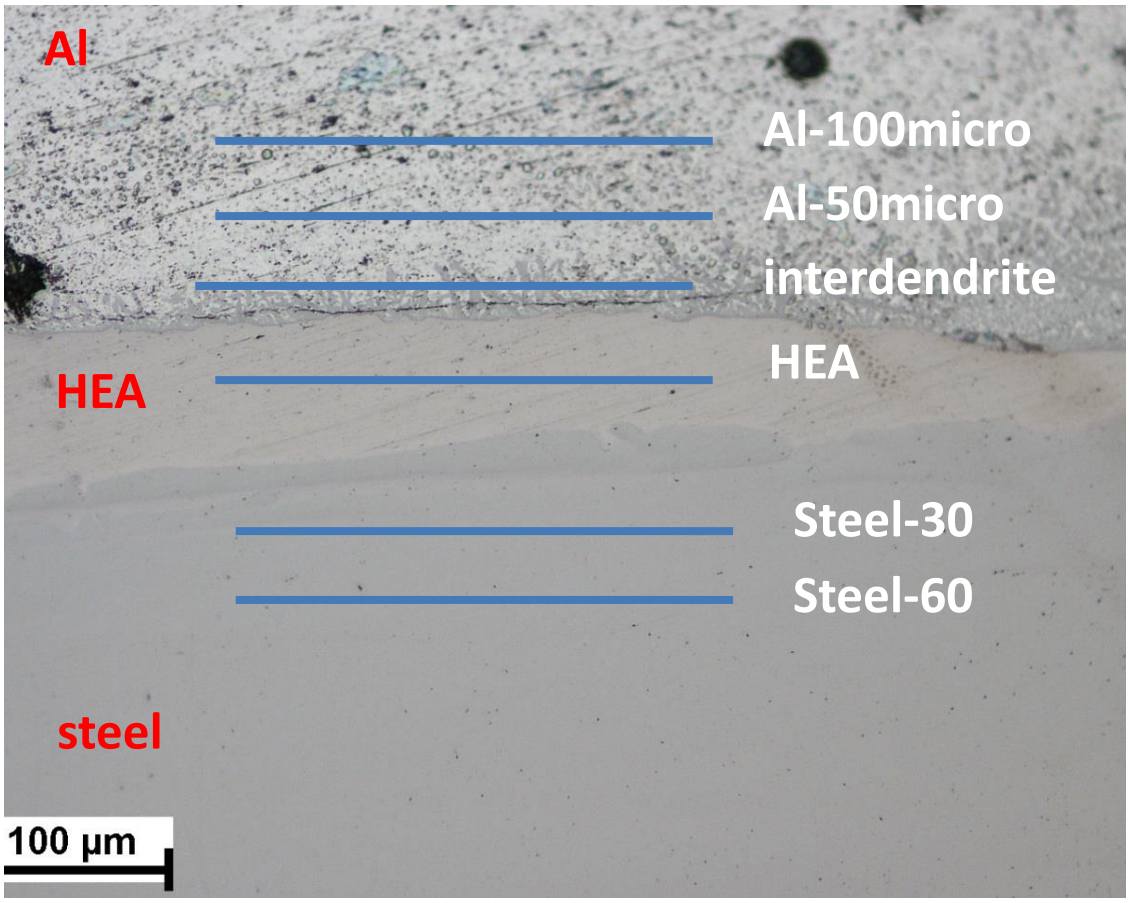

Figure 3.3. Measured location of the nano-indentation. From top to bottom, it is 1) Al side 100 micro away from the interface Al/HEA; 2) Al side 50 micro away from the interface Al/HEA; 3) Interdendrite layer; 4) HEA 5) Steel side away the interface steel/HEA; 6) Steel side away from the interface steel /HEA

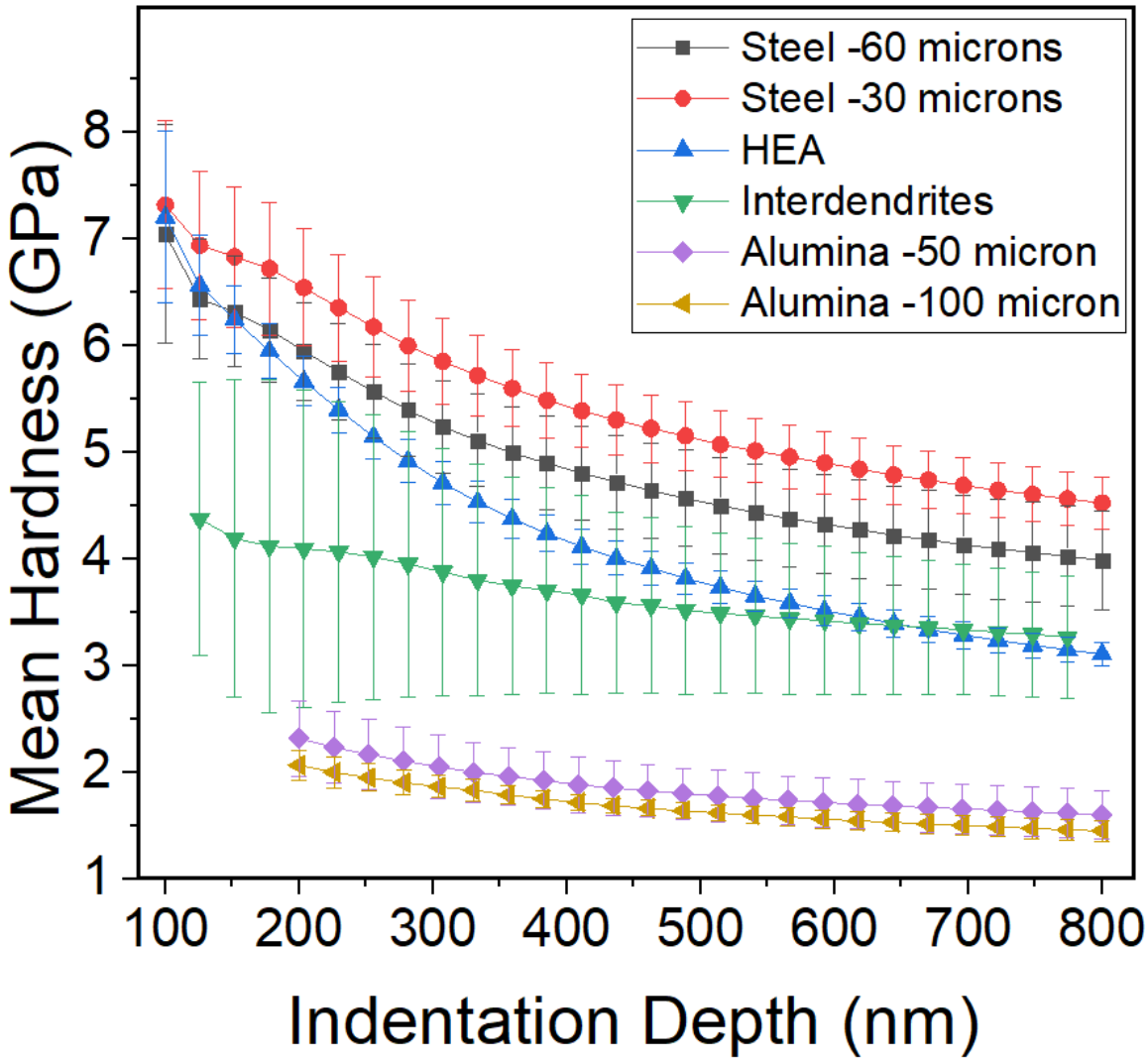

Figure 3.4. Mean hardness versus indentation depth curves with different location 1) Al side 100 micro away from the interface Al/HEA; 2) Al side 50 micro away from the interface Al/HEA; 3) Interdendrite layer; 4) HEA 5) Steel side away the interface steel/HEA; 6) Steel side away from the interface steel /HEA

(a) (b)

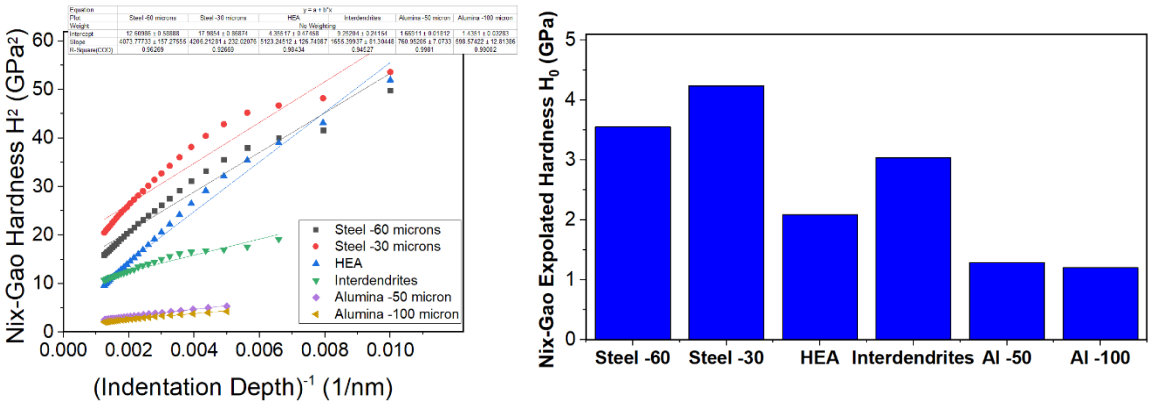

Figure 3.5. (a) Nix-Gao hardness versus (indentation depth)$^{-1}$; (b) Nix-Gao extrapolated hardness of 6 spots.

3. 4 Conclusions

In summary, the RSW results show that fusion zone between steel and HEA has formed, while little mixing is observed between the HEA and Al alloys. The failure of joining HEA and Al could be due to the high melting temperature of the HEA. The EDX results show that no diffusion happen between HEA and the Al alloys. The nanoindentation results suggest that intermetallics is formed between Al and the HEA on the Al side, which could worsen the mechanical property of the weld.

CHAPTER FOUR
HIGH-ENTROPY ALLOYS DESIGN WITH CALPHAD BASED HIGH THROUGHPUT METHOD AND EXPERIMENTS

4.1 Introduction

Multi-principal-element alloys (MPEA), or what are also called high-entropy alloys (HEAs) in many studies, have drawn a great deal of interest in the research field in recent years [2, 48-50]. Compared to conventional alloys which usually contains one principal element (e.g. Fe in steels, Al in aluminum alloys) and remain most of the properties of the base element, HEAs are defined as alloys that contain four or more elements with equimolar or near equimolar atomic percent of each element [2, 48]. This alloy design strategy is to maximize the configurational entropy of the solid solution phase and thus depress the formation of brittle intermetallics. Thus, HEAs possess a lot of unique outstanding properties such as high strength and good ductility at elevated temperature [51, 52], excellence fatigue resistance [10, 14, 53-56], creep resistance [57, 58], etc. The superior mechanical properties of HEAs, for example, the high strength and good plasticity of the refractory HEA NbTaTiV at elevated temperature [52], is attributed to the stable single solid solution microstructure without secondary phase segregation. Therefore, the design of HEAs with solid solution phases is one of the fundamental goals of HEAs design.

Generally, in the aspects of thermodynamics, the stability of a specific phase in an alloy system is determined by its corresponding Gibbs free energy (ΔG). For an alloys system,

when the Gibbs energy of solid solution phase (ΔG_{SS}) is lower than the Gibbs energy of intermetallics phases (ΔG_{IM}), the formation of solid solution phase will be more favorable and thus there will be a large probability to form solid solution alloys. And that's how the concept of high-entropy alloys works, since high configurational entropy is beneficial for the solid solution phase by reducing the overall Gibbs free energy of solid solution phases. Compared to time-consuming and costly experimental HEAs design, there are couple methods for HEAs design. The density function theory (DFT) method can provide detailed ΔG calculations of specific phases of an alloy system. However, due to the complicated phases in a HEAs system, it is highly computational resource consuming and restricted to limited atoms number (such as hundreds) [59-61]. Molecular dynamics (MD) method is another simulation method to calculate the ΔG of individual phases which can be under larger scale, but the application of this method to design HEAs is limited due to the lack of potential between elements [62, 63]. The formation rules, which are also called empirical rules, are popular criterions to predict whether specific compositions will form single phase or not [7, 64, 65]. This concept comes from the classic Hume-Rothery rules which are used to predict whether two metals are soluble [66, 67]. These parameters include mix of enthalpy, ΔH_{mix}, mix of entropy, ΔS_{mix}, and the extended Hume-Rothery rules such as atomic radius difference, electronegativity, and valence electron concentration difference [7].

Phase diagrams, which represents the state of a material as a function of its composition, temperature and pressure, are widely used as an effective and intuitive method for alloy design and further processing. The calculation of phase diagrams (CALPHAD) method,

which is adopted to be used as the main method for HEAs design in this study, is currently the only method to calculate phase diagram and predicting phase formation for multi-element alloy systems (element number > 3) [49, 68-70]. Although CALPHAD is argued that some complicated intermetallic phases with very low ΔG will be predicted as stable phase for HEAs in some studies [65, 71], CALPHAD has enough accuracy for real world applications, at the same time, avoid heavy experimental work and thus increase efficiency [72]. A lot of CALPHAD calculation effort has been put on the design and development of HEAs, especially one of the research focus is to look for single phase HEAs composition [50, 66, 67, 73]. Senkov et al conducted high throughput CALPHAD to calculate the phases of equimolar HEA compositions from 3 elements to 6 elements [50, 67]. He pointed out that the increase of elements of a HEA system will increase the configurational entropy but not necessarily promote the solid solution formation, since the more elements are involved in an alloy systems the higher possibility it will bring stable intermetallics [50]. This is one of the reasons that the definition of HEAs is broadened from equimolar or near equimolar, to alloy systems that each element has a molar fraction ranging from 5 – 35% [66]. There is also some examples showing that single phase formation can be found at the none-equimolar compositions, while the equimolar composition is not single phase, e.g. $Al_{2.8}$CoCrCuFeNi and AlCoCrCuFeNi [2]. In fact, the vast advantage of composition and phase space will not be fully utilized for HEAs if the focus is only on equimolar or near equimolar compositions. Nevertheless, limited studies focus on the overall single solid solution formation of a HEA system when each element is ranging from 5 – 35 at. %.

In this present study, a novel CALPHAD based high throughput calculation (HTC) method, which is implemented by Pandat software[74-76], will be applied to an element pool (Al, Cu, Fe, Ni, Mn, Co, Cr, Ti, Zr). The HEA screening process is shown in Figure 4.1. The first step is to pick up the elements pool of the simulation from the current PanHEA database. Then, high throughput calculations will be performed for solidification process of 221 compositions for each element combo. Afterwards, point calculation is performed to find out single phase compositions. Equilibrium solidification analysis will be conducted to study the singe phase temperature range for specific composition candidates. At the end, microstructural characterization experiments will be conducted to verify the simulation results. The single-phase solid solution ability of these 35 HEA systems will be discussed. It is the first study to propose for a high throughput CALPHAD calculation within an element pool with non-equimolar compositions, which offer a way to screen HEA compositions with targeted properties.

4.2 Methodology

4.2.1 High throughput calculations method based on CALPHAD

The traditional CALPHAD method is powerful to visualize the temperature vs ratio of single element changes [69]. However, it doesn't reflect the change of the whole system by one time. Senkov et al. evaluates over 13,000 equimolar alloy systems by CALPHAD, but the limitation of the work is that the binary and ternary databases are not fully described [50, 67].

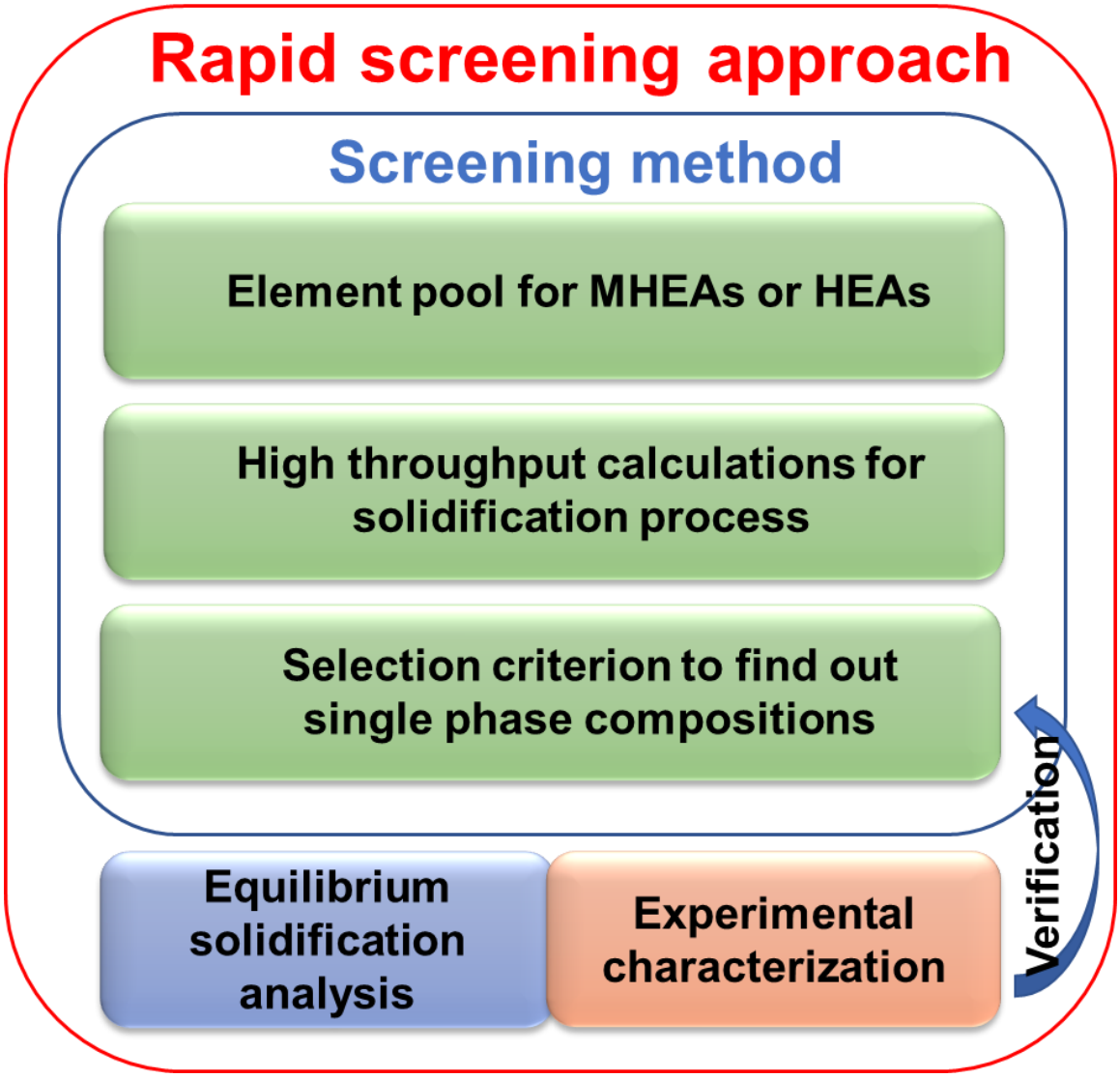

Figure 4.1. Equilibrium solidification analysis of Al2Cu10Fe20Ni30Mn38 by CALPHAD

The HTC method in present work, is implemented in a modulus in Pandat software with the database PanHEA2018_TH. In the HTC method, different step size can be set up and lead to different amount of calculation results. For example, for a 5 element system ABCDE, if we fix one of the element A as balance (which is mandatory in the software setting), let every other elements change from 5% to 35% with a step size of 10 (that means, the element changes from 5%, 15%, 25% to 35%), it will generate 221 results which fulfill the definition of HEAs. When the step size is set as 5, there could be 2075 results. When it goes to step size of 3, there will be over 10,000 calculation results. Data analysis will be critical after these high throughput calculation.

4.2 Methodology

4.2.1 High throughput calculations method based on CALPHAD

The traditional CALPHAD method is powerful to visualize the temperature vs ratio of single element changes [69]. However, it cannot see the whole system change by one time. Senkov et al. evaluates over 13,000 equimolar alloy systems by CALPHAD, but the limitation of the work is that the binary and ternary databases are not fully described [50, 67]. The HTC method in present work, is implemented in a modulus in Pandat software with the database PanHEA2018_TH. In the HTC method, different step size can be set up and lead to different amount of calculation results. For example, for a 5 element system ABCDE, if we fix one of the element A as balance (which is mandatory in the software setting), let every other elements change from 5% to 35% with a step size of 10 (that means, the element changes from 5%, 15%, 25% to 35%), it will generate 221 results which fulfill

the definition of HEAs. When the step size is set as 5, there could be 2075 results. When it goes to step size of 3, there will be over 10,000 calculation results. Data analysis will be critical after these high throughput calculation.

4.2.2 Credibility of the HTC and CALPHAD simulations through Pandat

The CALPHAD method is capable of producing reliable and accurate enough phase diagram results. Its credibility is almost fully based its thermodynamic database, since CALPHAD phase diagram can be regarded as the extrapolation of the thermodynamic binary descriptions and ternary descriptions [69]. Senkov et al comes up with a credibility criteria for CALPHAD calculation in multi-element alloy system with two parameters: f_{AB}, the fraction of fully thermodynamically assessed binary systems, and, f_{AT}, the fraction of fully thermodynamically assessed ternary systems [50]. If all relevant binary and ternary description are included in the database, then the $f_{AB} = 1$ and $f_{AT} = 1$, and the credibility of the calculation results on this system is considered to be high. In this present work, the PanHEA_2018_TH database contains all the binary and ternary descriptions between the selected elements (Al, Cu, Co, Cr, Fe, Ni, Mn, Ti, Zr). Therefore, the credibility of the CALPHAD calculations is considered to be high and reliable.

4.2.3 Experimental details

The HEAs were fabricated by arc melting. The purity of all the elements is larger than 99.9%. To ensure the homogeneity, the alloy ingots were flapped and melted at least 5 times. For the heat treated Al2Cu10Fe20Mn38Ni30, the heat treatment condition was

900°C for 3 hours. The microstructure and elemental distribution of the HEAs were examined with scanning electron microscopy (SEM, ZEISS EVO) couple with energy-dispersive spectroscopy (EDS). The crystal structure was examined with the X-ray diffraction (XRD, Panalytical Empyrean). The samples for these experiments were polished by the vibration polishing method after grinding with the 1200 grit SiC paper.

4.3 Results

4.3.1 HTC and CALPHAD results analysis

In the current work, 221 solidification calculations, with a step size of 10, are conducted for each element combo among Al-Cu-X-X-X (X = Co, Cr, Fe, Ni, Mn, Ti, Zr), totally there 7,735 calculations for the initial procedure. The numbers of single FCC, BCC, and HCP generated by each element combo are shown in Table 4.1. 12 out of 35 element combos are found to have single FCC compositions, 3 of them could potentially have BCC compositions, and 0 HCP compositions are found through the simulation. Compositions among the element pool show a stronger tendency to form FCC single phase, compared with forming BCC and HCP single phase. From the table, the Al-Cu-Fe-Ni-Mn, Al-Cu-Fe-Co-Ni, and Al-Cu-Co-Ni-Mn element combos exhibit 40, 36, and 34 FCC single phase compositions, excessively higher than other element combos. The goal of this work is to screen the alloy system with strongest FCC single phase formation ability, the discussion will be focus on single FCC phase.

Table 4.1. HTC results containing the numbers of types of single phases (FCC, BCC, and HCP) with step size of 10.

	Elements					FCC	BCC	HCP
1	Al	Cu	Cr	Co	Fe	1	3	0
2	Al	Cu	Cr	Co	Ni	8	0	0
3	Al	Cu	Cr	Co	Ti	0	0	0
4	Al	Cu	Cr	Co	Zr	0	0	0
5	Al	Cu	Cr	Co	Mn	1	0	0
6	Al	Cu	Cr	Fe	Ni	9	0	0
7	Al	Cu	Cr	Fe	Ti	0	0	0
8	Al	Cu	Cr	Fe	Zr	0	0	0
9	Al	Cu	Cr	Fe	Mn	0	5	0
10	Al	Cu	Cr	Ni	Ti	0	0	0
11	Al	Cu	Cr	Ni	Zr	0	0	0
12	Al	Cu	Cr	Ni	Mn	3	0	0
13	Al	Cu	Cr	Ti	Zr	0	0	0
14	Al	Cu	Cr	Ti	Mn	0	0	0
15	Al	Cu	Cr	Zr	Mn	0	0	0
16	Al	Cu	Co	Fe	Ni	36	1	0
17	Al	Cu	Co	Fe	Ti	0	0	0
18	Al	Cu	Co	Fe	Zr	0	0	0
19	Al	Cu	Co	Fe	Mn	11	0	0
20	Al	Cu	Co	Ni	Ti	2	0	0
21	Al	Cu	Co	Ni	Zr	0	0	0
22	Al	Cu	Co	Ni	Mn	34	0	0
23	Al	Cu	Co	Ti	Zr	0	0	0
24	Al	Cu	Co	Ti	Mn	0	0	0
25	Al	Cu	Co	Zr	Mn	0	0	0
26	Al	Cu	Fe	Ni	Ti	7	0	0
27	Al	Cu	Fe	Ni	Zr	0	0	0
28	Al	Cu	Fe	Ni	Mn	40	0	0
29	Al	Cu	Fe	Ti	Zr	0	0	0
30	Al	Cu	Fe	Ti	Mn	0	0	0
31	Al	Cu	Fe	Zr	Mn	0	0	0
32	Al	Cu	Ni	Ti	Zr	0	0	0
33	Al	Cu	Ni	Ti	Mn	1	0	0
34	Al	Cu	Ni	Zr	Mn	0	0	0
35	Al	Cu	Ti	Zr	Mn	0	0	0

The Al-Cu-Fe-Ni-Mn combo has the most FCC single phase number among the 35 element combos, which is considered to have the strongest ability to form FCC single phase among the 35 element combos. Further calculation with a step size of 5 are conducted on the selected Al-Cu-Fe-Ni-Mn system.

4.3.2 Equilibrium solidification analysis of selected candidate

The equilibrium solidification simulation of a selected composition candidate, Al2Cu10Fe20Ni30Mn38, is shown in Figure 4.2. The y axis represents the fraction of phases, while the x axis represents the Temperature change. From the right side to the left side of the figure, it can be regarded as an alloy from the high temperature liquid state to the low temperature solid state. It can be observed that the during the solidification process, FCC structure is the first solid phase forming at 1219°C and finish at 1131°C. The FCC single phase structure remains until the temperature decreases to 415°C. Then B2 phase starts to form. Then BCC and some intermetallic phases will be formed later under equilibrium condition. The equilibrium solidification result shows a promising possibility of the Al2Cu10Fe20Ni30Mn38 to be FCC single phase. This result also gives us a guidance of how to select the homogenization temperature. In this case, 900 °C for 4 hours could be a suggested heat treatment condition in the later experimental verification part. This HEA composition also shows a much lower solidus melting temperature, compared to a lot of the reported HEAs, such as Al-Co-Cr-Fe-Ni and refractory HEA [3].

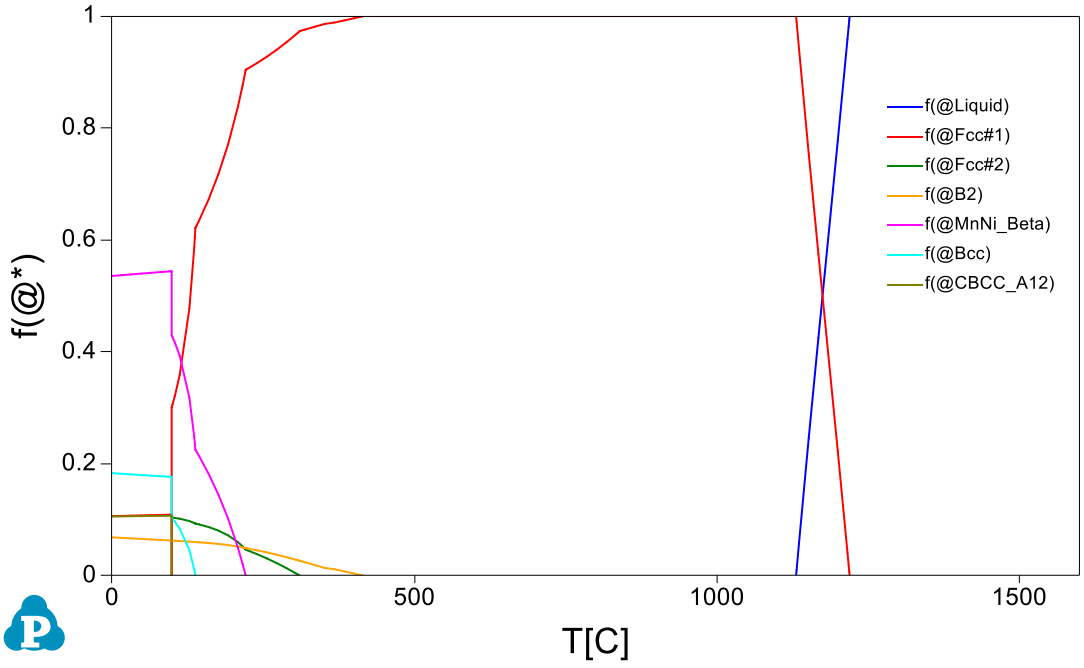

Figure 4.2. Equilibrium solidification analysis of Al2Cu10Fe20Ni30Mn38 by CALPHAD

4.3.3 Experimental verification

In this work, the designed alloys Al2Cu10Fe20Ni30Mn38 was fabricated and further heat-treated. After heat treatment and polish of samples, XRD, SEM and EDX characterization are performed on the selected composition.

From the XRD pattern as shown in Figure 4.3, the crystal structure of the heat treated Al2Cu10Fe20Ni30Mn38 were FCC structure where typical (111) (200) (220) and (311) FCC peaks were shown. No second phase peaks are observed in the XRD pattern. The XRD results suggest the composition has a FCC single phase.

Figure 4.4 demonstrates the microstructure of the heat-treated Al2Cu10Fe20Ni30Mn38. A dendrite structure is observed. The spot EDX locations are also shown in the Figure 4.4. The spot EDX results in Table 4.2 show that the Al is less than the nominal compositions, while the Fe has more than the nominal composition. This could be due to evaporation of aluminum during fabrication. After all, the mean value of the chemical composition of the Al2Cu10Fe20Ni30Mn38 sample is comparable with the nominal composition. The standard deviation of the EDX result all less than 2%, which exhibits that the elements are homogeneously distributed after heat treatment.

From the CALPHAD line analysis shown in Figure 4.2, the Al2Cu10Fe20Ni30Mn38 is predicted to have FCC single phase. The experiment results further verify that this composition after heat treatment will have FCC single phase. The experimental results agreed well with the CALPHAD prediction.

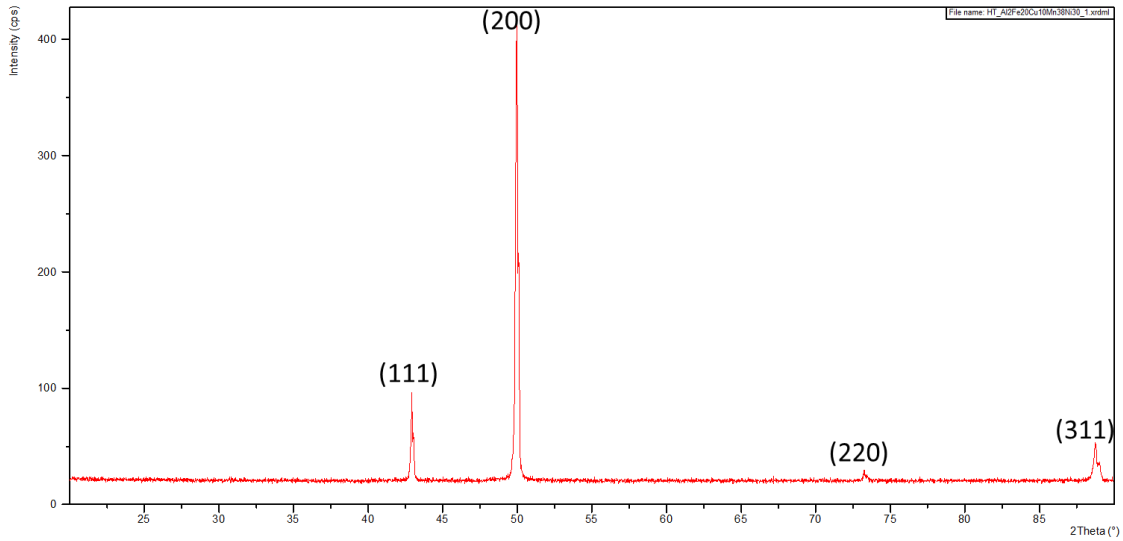

Figure 4.3. XRD pattern of Al2Cu10Fe20Ni30Mn38 by CALPHAD

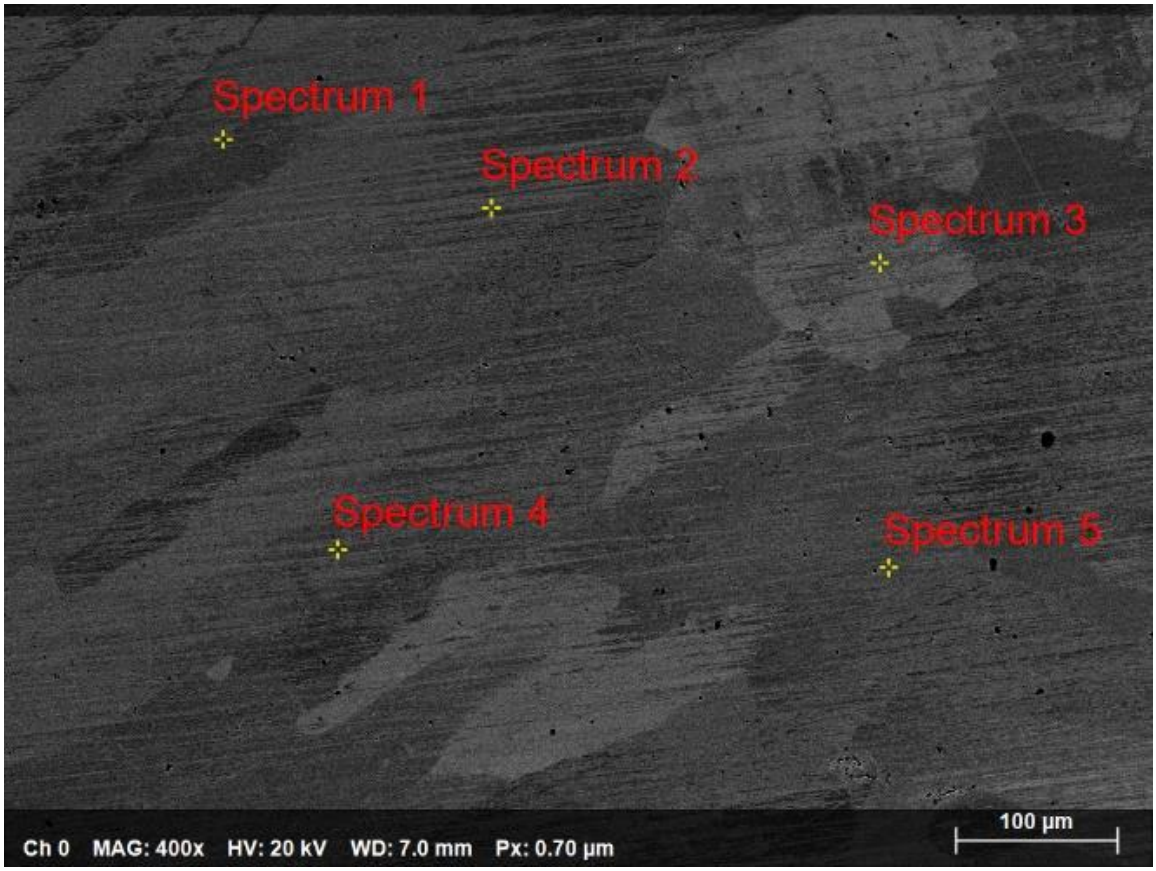

Figure 4.4. SEM image of the Al2Cu10Fe20Mn38Ni30

Table 4.2. Chemical compositions of Al2Cu10Fe20Mn38Ni30 by EDX

Spectrum	Al	Mn	Fe	Ni	Cu
Spectrum 5	1.56	35.13	23.86	29.31	10.14
Spectrum 1	1.62	36.35	20.92	29.59	11.51
Spectrum 2	1.56	35.64	22.47	29.53	10.79
Spectrum 3	1.49	35.68	22.36	29.60	10.86
Spectrum 4	1.47	36.03	21.30	29.78	11.41
Mean	1.54	35.77	22.18	29.56	10.94
STDVEA	0.06	0.46	1.15	0.17	0.55

4.4 Discussion

A screening methodology developed in this present study allows us to quickly identify, screen and analyze around 10,000 MPEA compositions at non-equiatomic compositions for required microstructure and specific melting ranges. The thermodynamic properties, such as phase present, solidus temperature, and liquidus temperature, can be determined by each alloy composition using CALPHAD calculations with Pandat software and PanHEA database developed by CompuTherm LLC. The screening process, properties calculation and further analysis are facilitated with Pandat.

4.4.1 Distribution of solid solution phase by their crystal structure and elements

Among FCC, BCC and HCP single phases, FCC has the highest count of the calculated compositions of 153, BCC is the second of 9, while no HCP single phase is found in the calculation. The detail count of compositions of each single phase is shown in Figure 4.5. The observed distribution of single phases of the calculated Al-Cu-X-X-X (X = Co, Cr, Fe, Ni, Mn, Ti, Zr) can be correlated with the number of elements having these respective crystal structures. Of the 9 elements in the present study, 6 of them have FCC structure (Al, Cu, Ni, Co), 5 of them have BCC structure (Fe, Mn, Cr), 3 of them have HCP structure (Co, Zr, Ti) at room temperature [77]. In the case of fixing the Al and Cu in the alloy system, the ratio of FCC elements increases, which promote the formation of FCC single phase.

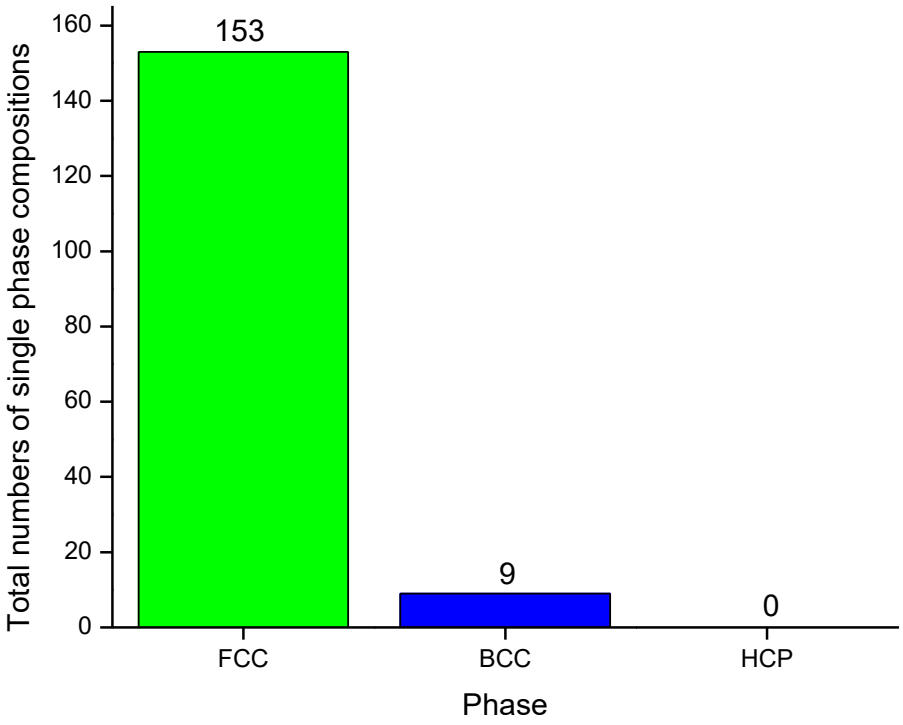

Figure 4.5. Counts of single FCC, BCC and HCP solid solution phases

Different elements contribute differently in the Al-Cu-X-X-X (X = Co, Cr, Fe, Ni, Mn, Ti, Zr) system. Figure 4.6 Shows the counts of FCC single phase per element. Zr has 0 count in the calculated FCC single phase compositions. As a BCC promoter, Zr in the HEA composition more tend to form BCC rather than FCC, which is well reported in reported studies [77-79]. Ni has the highest count to promote FCC in our current calculation.

4.4.2 Liquidus melting temperature distribution of the Al-Cu-Fe-Ni-Mn system

One of the important purpose of the present HEA design is to find HEA composition that with high possibility to form FCC single phase while have a melting temperature between Al-alloy and steel. Among our 35 Al-Cu-X-X-X (X = Co, Cr, Fe, Ni, Mn, Ti, Zr) calculated system, the Al-Cu-Fe-Ni-Mn has the highest amount of FCC single phase in the calculation with step size of 10, as shown in Table 4.1. Having a further look of the melting temperature of the FCC single phase compositions in the Al-Cu-Fe-Ni-Mn system is necessary. Figure 4.7 shows the liquidus melting temperature range of the 275 calculated FCC single-phase compositions of Al-Cu-Fe-Ni-Mn system with step size of 5 calculation. The whole melting range is between 1,015 °C to 1,332 °C, which is obviously lower than the Al0.1CoCrFeNi and Al0.3CoCrFeNi which are around 1,400 °C [49]. Since the alloy system contains large amount of Al and Cu, the system could have lower liquidus melting point than most of the reported HEAs which are drawn more attention in elevated temperature application., while at the same time maintaining the ability to form FCC single phase.

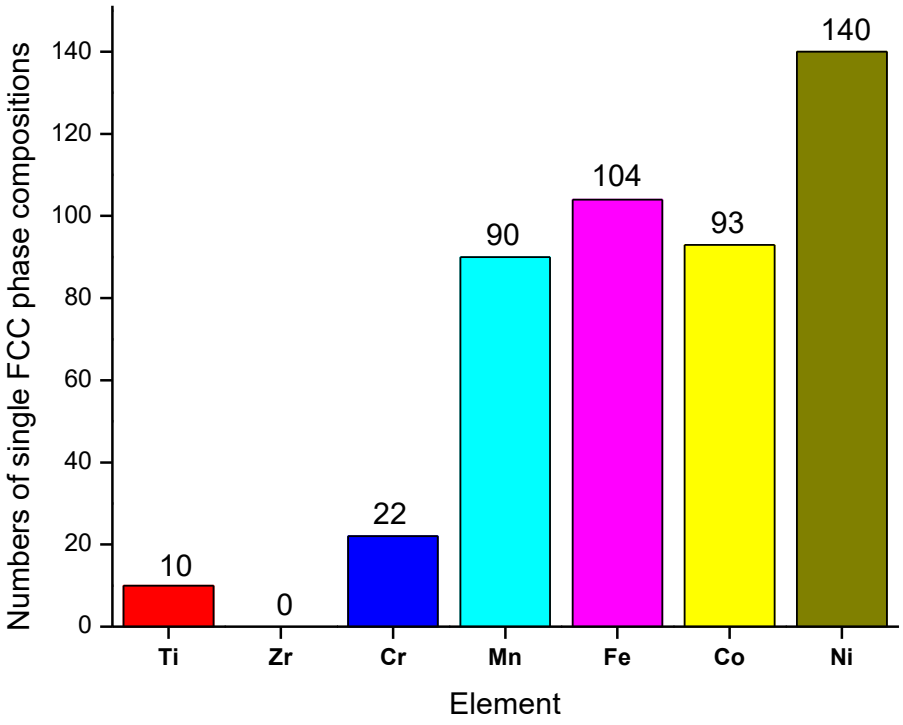

Figure 4.6. Counts of single FCC phase compositions per element

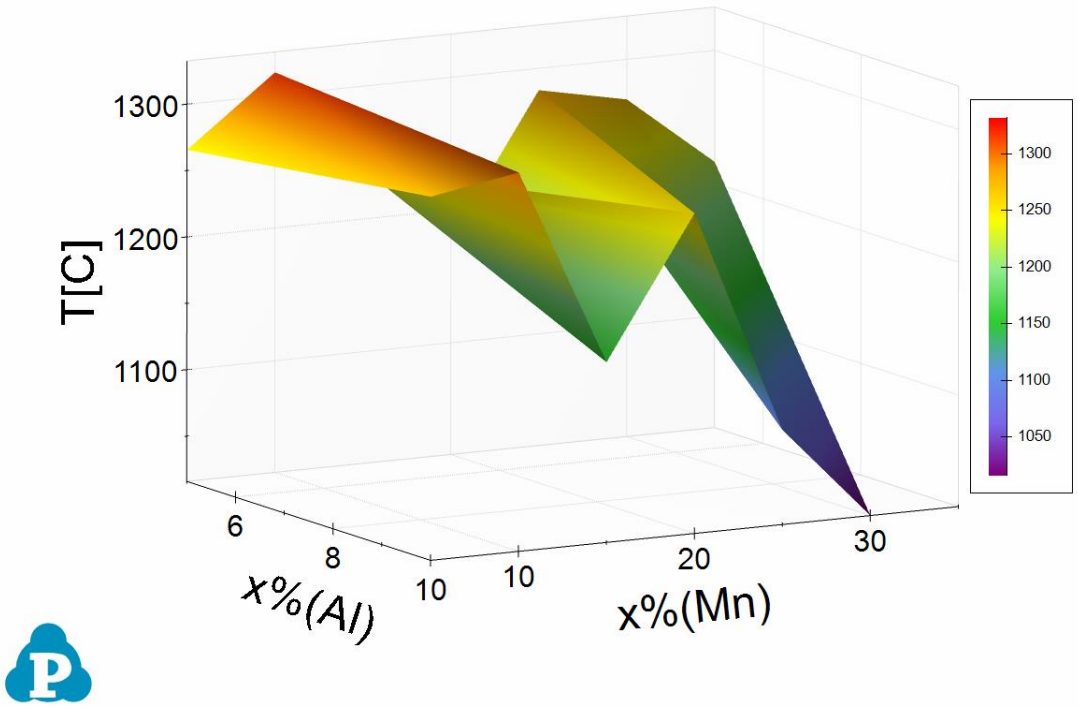

Figure 4.7. Temperature distribution of the 275 calculated FCC single-phase compositions of Al-Cu-Fe-Ni-Mn system.

4.5 Conclusions

In summary, a novel simulation method to design and develop HEAs is proposed with high-throughput CALPHAD. It can be concluded in the following:

1. In the current work, the phase stability of 35 HEA systems from Al-Cu-X-X-X (X=Co, Cr, Fe, Ni, Mn, Ti, and Zr) is investigated by the high-throughput CALPHAD method. The Al-Cu-Fe-Ni-Mn is found to have the strongest for single FCC phase formation ability among the 35 systems. Compared with the classic Al-Co-Cr-Fe-Ni, the Al-Cu-Fe-Ni-Mn HEA system shows a better FCC single phase formation ability.
2. Further simulation with more data result suggests Al-Cu-Fe-Ni-Mn has 275 FCC single-phase compositions out of 2075 data points. The solidus temperature range of the calculated FCC single-phase compositions are between 1015°C to 1332°C.
3. Suggested candidate composition Al2Cu10Fe20Ni30Mn38 is obtained by the CALPHAD line analysis. This composition is fabricated by arc-melter and heated-treated. The XRD, SEM and EDX results confirmed this composition has FCC single phase structure.

CHAPTER FIVE
DISSIMILAR WELDING BETWEEN AL-ALLOYS AND STEEL WITH AL2CU10FE20NI30MN38 HIGH-ENTROPY ALLOYS

5.1 Introduction

Weight reduction of component is always an important topic in the aerospace and automotive industries. Considering the aspects of performance, cost, and weight, introducing aluminum alloys to steels body are one of the most attractive alloy combinations to reduce weight in machine bodies. Owing to efficiency and volume of production, resistance spot welding (RSW) is one of the most important joining methods in automotive industries. To produce the hybrid structure of Aluminum alloys and steels, a technology to make dissimilar Al/Fe joints is needed, especially with RSW since it is very commonly used in the industries. However, due to the great intrinsic difference in thermal, electrical and mechanical properties, brittle intermetallic compounds are always formed in the welding joint between aluminum alloys and steels which will lead to degradation of mechanical properties [34-42]. Shanglu et al. investigated the welding of the aluminum alloy, 6061 - T6 [Al - 0.04Cr - 0.3Cu - 0.7Fe - 1.0Mg - 0.15Mn - 0.6Si - 0.15Ti - 0.25Zn, weight percent (wt.%)], to zinc - coated steel (0.05 to 0.25% carbon content) by the cold - metal - transfer method [41]. Cracking and lack of fusion between steels and aluminum alloys are observed. Torkamany et al. studied the welding of the carbon steel (Fe - 0.4Mn - 0.04C wt.%) to 5754 aluminum alloy (Al - 0.12Si - 0.04Cu - 0.25Mn - 3.009Mg - 0.08Cr - 0.006Ni - 0.37Fe wt.%) by Nd with laser welding [39]. Pores and pre-crack are found, along with the Fe - Al intermetallics. Ranfeng et al. reported the resistance - spot welding

on the aluminum alloy, A5052 (Al - 2.2Mg - 0.27Fe - 0.19Cr - 0.09Si - 0.049Mn - 0.027Cu - 0.005Zn wt.%), to steel SPCC (Fe - 18Cr - 0.85Si - 1.25Mn - 0.06C - 0.04P - 0.02S wt.%), and austenitic - stainless steel SUS304 (Fe - 18.0Cr - 0.85Si - 1.25Mn - 0.06C - 0.04P - 0.02S - 8.0S wt.%) [36]. After the tensile tests, the strength of aluminum self - weld joint, A5052/A5052, is higher than the joints of A5052/SPCC and A5052/SUS304, which indicates that the joints between aluminum alloys and steels are not favorable. Satonaka et al. developed a new method termed the resistance - spot welding with a cover plate between the aluminum and electrode, to obtain higher temperature in the weld [43]. Ranfeng et al. then used this method to weld the aluminum A5052 to steel SPCC and steel SUS304 and obtain joints between the aluminum and steels with higher strength [35]. However, a large amount of Fe - Al intermetallics are still formed, which greatly affect the mechanical property of the joints.

One of the directions of the Fe - Al welding is to put interlayer. HEAs, are come up with as the interlayer materials. In chapter 3, RSW trials have been conducted with Al0.3CoCorFeNi HEA. However, lack of mixing is observed between HEA and Al alloys, where the failure initiates during mechanical tests. To solve this problem, in chapter 4, a FCC single phase HEA composition with lower liquidus melting temperature, Al2Cu10Fe20Ni30Mn38, is developed via high throughput CALPHAD method. In this chapter, welding trial will be conducted with this new HEA Al2Cu10Fe20Ni30Mn38. The solidification process will be predicted by CALPHAD with Scheil-Gulliver model to better understand the solidification range and phase formation of the nuggets [68, 80, 81]. A model which is come up with by Sindo Kou will be applied in this study to understand the

solidification susceptibility [82-95]. Finally, based on the solidification range of the welding nugget, future HEA candidate compositions are suggested after HEA modification.

5.2 Materials and Methodology

5.2.1 Materials

The materials used in this investigation were JAC980 high-strength low-alloy steel with 1.0 mm thickness, 5754 aluminum alloys with 2.0 mm thickness, and Al0.2Cu10Fe20Ni30Mn38 HEA interlayer. The chemical composition of JAC980 steel and 5754 aluminum alloys are given in Table 3.1.

5.2.2 Experimental details

The Al0.2Cu10Fe20Ni30Mn38 HEAs were fabricated by arc melting. The purity of all the elements is larger than 99.9%. To ensure the homogeneity, the alloy ingots were flapped and melted at least 5 times. After that, the Al0.2Cu10Fe20Ni30Mn38 is sealed in vacuum glass tube and heat treated at 900°C for 3 hours. The microstructure and elemental distribution of the HEAs were examined with scanning electron microscopy (SEM, ZEISS EVO) couple with energy-dispersive spectroscopy (EDS). The crystal structure was examined with the X-ray diffraction (XRD, Panalytical Empyrean). The HEA foils were prepared with up to 1200 grits to remove surface oxidation and cleaned by acetone.

Resistance spot welding were performed in the condition of 12kA, 1100lb, 10cycles. The top and button electrodes are both Cu-Zr, 2” radius nose. The thickness of the

Al0.2Cu10Fe20Ni30Mn38 HEA foil is 0.42 mm. The schematic of the cladding of the three materials is shown in Figure 5.1.

5.2.3 Solidification and phase analysis with CALPHAD

To better understand the phase formation and solidification process of the welding nugget, solidification simulation will be conducted via Pandat software with PanHEA 2019 database. A Scheil-Gulliver model will be applied during the simulation, as it assuming a non-equilibrium solidification process with very fast cooling rate [68, 80, 81]. To better understand the microstructure of the welding nugget, a phase construction after the solidification process ends will be calculated. The input elemental composition information will come from the EDS experiments.

5.2.4 A model to evaluate the susceptibility of solidification cracking

Cracking especially solidification cracking happens very often during dissimilar welding. To evaluate the susceptibility of solidification cracking, a criterion for cracking during solidification will be calculated for the nugget.

In the paper " A criterion for cracking during solidification" 2015, Sindo Kou derive the below equation [82]:

$$\left\{ \underbrace{\frac{d\varepsilon_{local}}{dT}}_{\text{(separation)}} > \underbrace{\sqrt{1-\beta}\frac{d\sqrt{f_S}}{dT}}_{\text{(growth)}} + \frac{1}{(dT/dt)}\frac{d}{dz}\underbrace{\left[\left(1-\sqrt{1-\beta}\sqrt{f_S}\right)v_z\right]}_{\text{(feeding)}} \right\}_{\sqrt{f_S}\to 1} \quad (8)$$

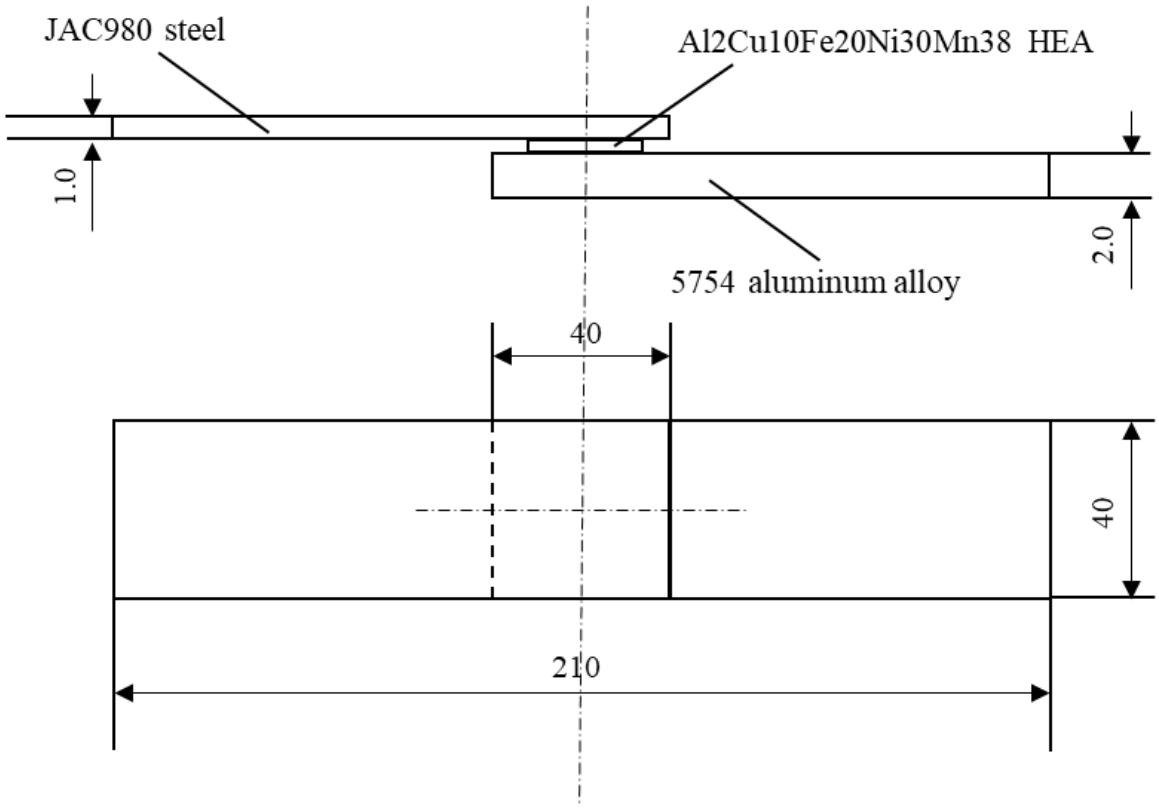

Figure 5.1. Geometry and dimensions of specimens for welding (not to scale, dimensions in mm)

And the criterion index is $|dT/d(f_S^{1/2})|$ near $(f_S)^{1/2} = 1$, where f_S is the fraction of solid, and T is the temperature. The susceptibility of solidification cracking increases as the $|dT/d(f_S^{1/2})|$ near $(f_S)^{1/2} = 1$ increases [82]. Figure 5.2 shows an example of different $|dT/d(f_S^{1/2})|$ near $(f_S)^{1/2} = 1$ values of (a) Al alloy A356; (b) Al alloy A206. A lower $|dT/d(f_S^{1/2})|$ near $(f_S)^{1/2} = 1$ represents that near the end of the solidification, the channel between grains will be shorter. Liquid feeding will be easier and less likely to cause crack initiation and crack propagation. On the contrary, the channel between grains will be longer when $|dT/d(f_S^{1/2})|$ near $(f_S)^{1/2} = 1$ increases, which will make it harder for feeding and thus more likely for crack initiation and propagation. In the current study, the $|dT/d(f_S^{1/2})|$ near $(f_S)^{1/2} = 1$ will be calculated with the solidification curve mentioned above.

In the current work, this model will be applied to evaluate the cracking susceptibility of the welding nugget. The nugget composition will be obtained from the EDX results after welding test. The fraction of solid versus temperature curve will be obtained from the solidification analysis via CALPHAD. The criterion index $|dT/d(f_S^{1/2})|$ near $(f_S)^{1/2} = 1$ will be calculated. In the discussion part, new HEA compositions will be discussed to lower the cracking susceptibility.

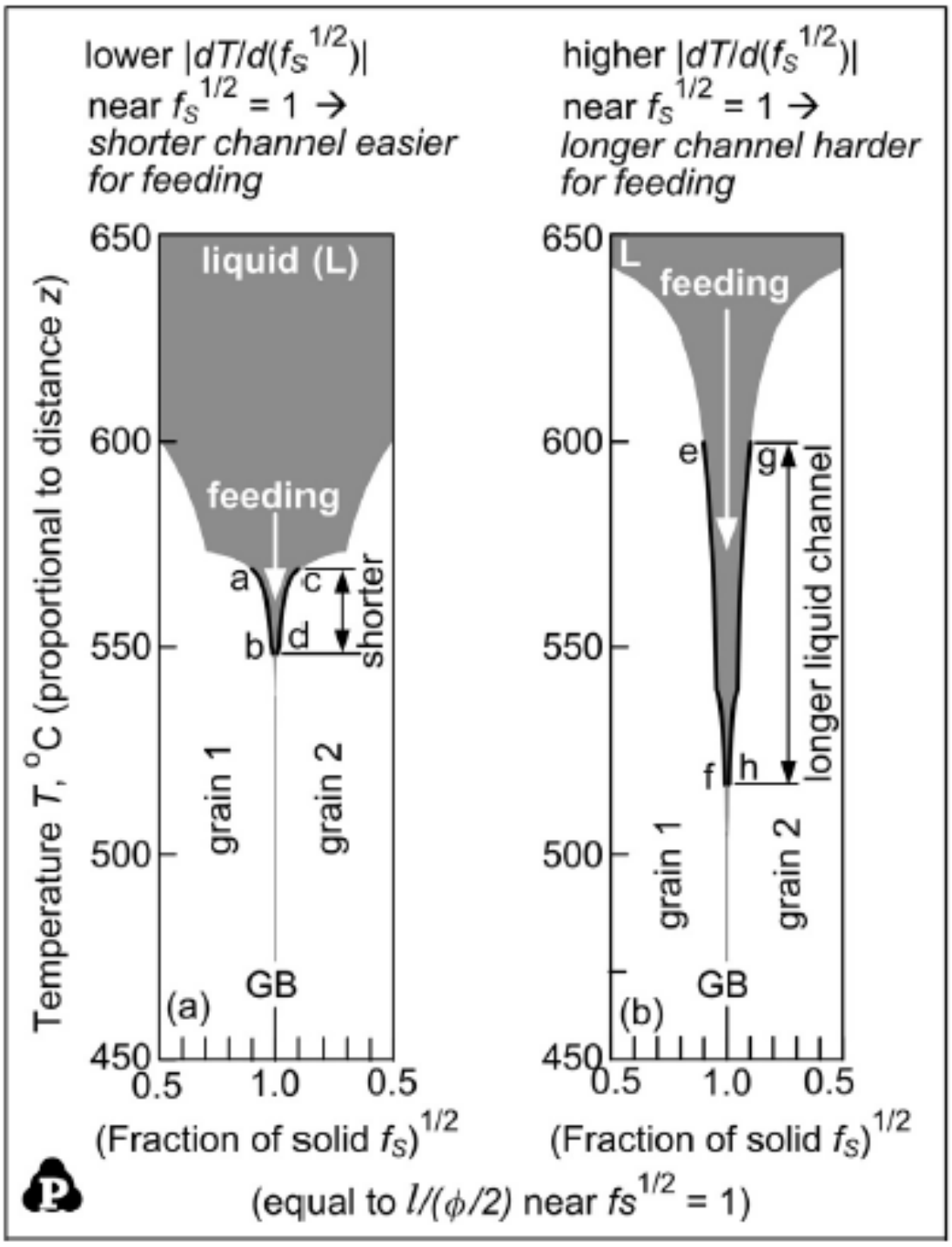

Figure 5.2. Effect of $|dT/d(f_S^{1/2})|$ near $(f_S)^{1/2} = 1$ on liquid feeding: (a) Al alloy A356; (b) Al alloy A206. The S/L interfaces can be approximated by curves of T vs. $(f_S)^{1/2} = 1$ especially near the grain boundary GB, where $(f_S)^{1/2} = 1$. Note that ac = eg and bd = fh [82].

5.3 Experimental Results

5.3.1 Microstructure of welding joint

Figure 5.3 shows the appearance of the joint obtained at 12 kA for 10 cycles. Compared to what are presented in chapter 3, the joint shows a mixing of the three materials. Cracking and pores can be observed. The cracking direction is along with the applied force direction from the electrodes. The pores are observed in the aluminum alloys side which could highly be susceptible to be happen due to the re-solidification of the aluminum alloys from liquid state during welding. It is the first time observing a mixing zone of the steel, HEA layer, and the aluminum alloys.

The SEM microstructure is exhibited in the Figure 5.4. From Figure 5.4(a) and Figure 5.4(b), a dendritic structure was observed at the center of the nugget. As at a higher magnitude, Figure 5.4(c) exhibits a spinodal decomposition phenomenon, which suggests that multi phases may exist in the welding joint.

The EDS results which point to the marked spot from Figure 5.3 is shown in Table 5.1. Spot 2 contains as high as 90.8% Al, which refers to the 5754 base materials. Spot 4 shows a composition that close to the Al2Cu10Fe20Ni30Mn38 HEA composition. The spots 1, 3, 5a, 5b, 6a, and 6b show close values of mixing of Mg, Al, Mn, Fe, Ni, and Cu. Even though the spot 1, 3, 5a, 5b, 6a, and 6b are measured from different location of the nugget, which suggests that the nugget composition is relatively unified. Further evaluation of the welding nugget will be in the discussion part.

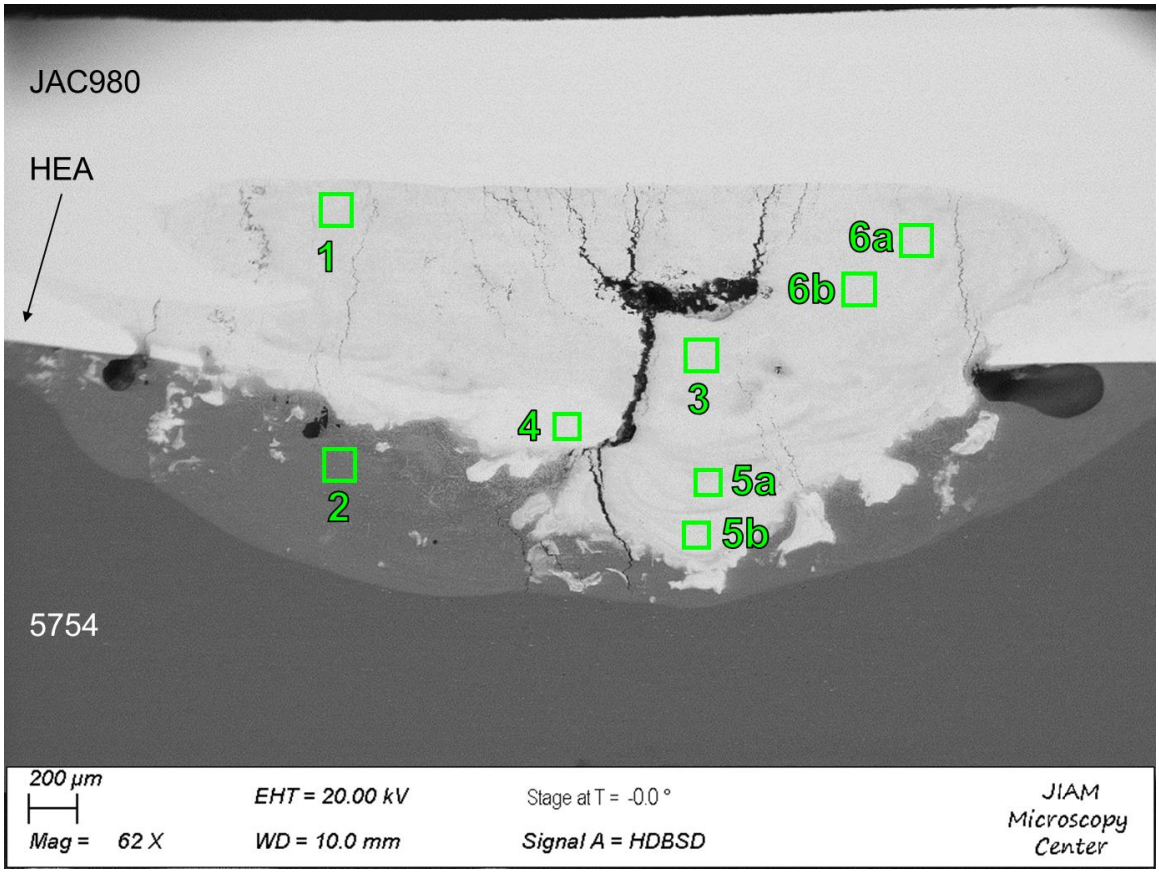

Figure 5.3. Appearance of the JAC 980 steel – HEA – 5754 aluminum welding joint.

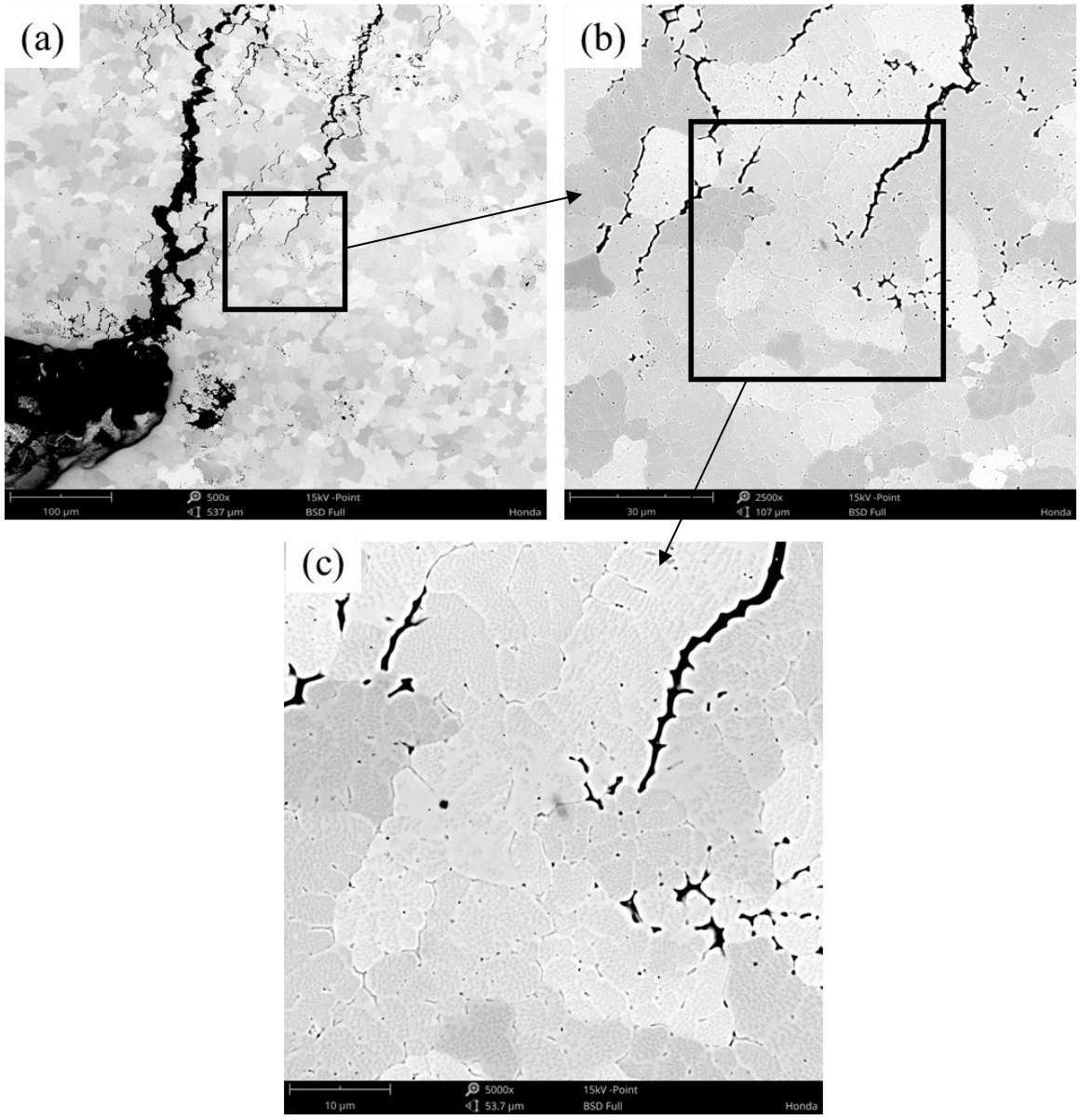

Figure 5.4. (a) SEM image of the JAC 980 steel – HEA – 5754 aluminum welding joint; (b) selected area from (a); (c) selected area from (b).

Table 5.1. Chemical composition of spots that shown in Fig 5.2.

Numbered Location	Mg	Al	Mn	Fe	Ni	Cu
1	0.67	21.5	16.5	44.1	12.5	4.33
2	4.16	90.8	1.77	1.26	1.40	0.56
3	0.71	21.4	16.3	44.9	12.2	4.25
4	0.24	6.91	13.5	66.0	9.55	3.29
5a	0.61	21.1	16.5	44.7	12.5	4.25
5b	0.66	20.0	17.0	44.6	12.9	4.40
6a	0.61	18.4	16.7	47.0	12.6	4.34
6b	0.58	20.2	16.3	45.9	12.4	4.23

5.4 Discussion

5.4.1 Solidification and phase analysis by CALPHAD

To start the simulation of solidification, first of all, the nugget composition needs to be obtained from the EDX results. Here, the spots 1, 3, 5a, 5b, 6a, and 6b from Figure 5.3 are selected since they are the measurement of the nugget. The average value and standard deviation of the data of the selected spots are shown in Table 5.2. The standard deviation of the data are small enough to make sure the average value reflects the chemical composition of the whole nugget during the CALPHAD simulation.

Figure 5.5 presents the simulated solidification path of the nugget composition which listed in the Table 5.2, using the Scheil-Gulliver model (assuming a very high cooling rate). Following the blue line in Figure 5.5, the solidification path of the nugget can be forecast, which is Liquid → Liquid + BCC → Liquid + BCC + B2 → Liquid + BCC + B2 + FCC → Liquid + BCC + B2 + FCC + Laves phase. The primary solidified phase is BCC. As the content of Al reaches around 20%, the nugget compositions has disordered BCC and ordered B2, which is consistent with many published experimental results with AlxCoCrFeNi [96-98]. The fraction of final possible phases obtained from the simulation results is shown in Table 5.3. The final nugget composition is predicted to have ~29% FCC, ~49.6% BCC, ~19.6% B2 and some minor phases. The high amount of the FCC, BCC and B2 phases are related to the microstructure in Figure 5.4. It should be notice that the high amount of B2 phase (19.58%) could lead to a brittle mechanical behavior of the welding joint.

Table 5.2. The average chemical compositions of selected spots

Element	Mg	Al	Mn	Fe	Ni	Cu
Avg at. %	0.64	20.4	16.6	45.2	12.5	4.3
Standard deviation	0.048166	1.174166	0.266458	1.062073	0.231661	0.066933

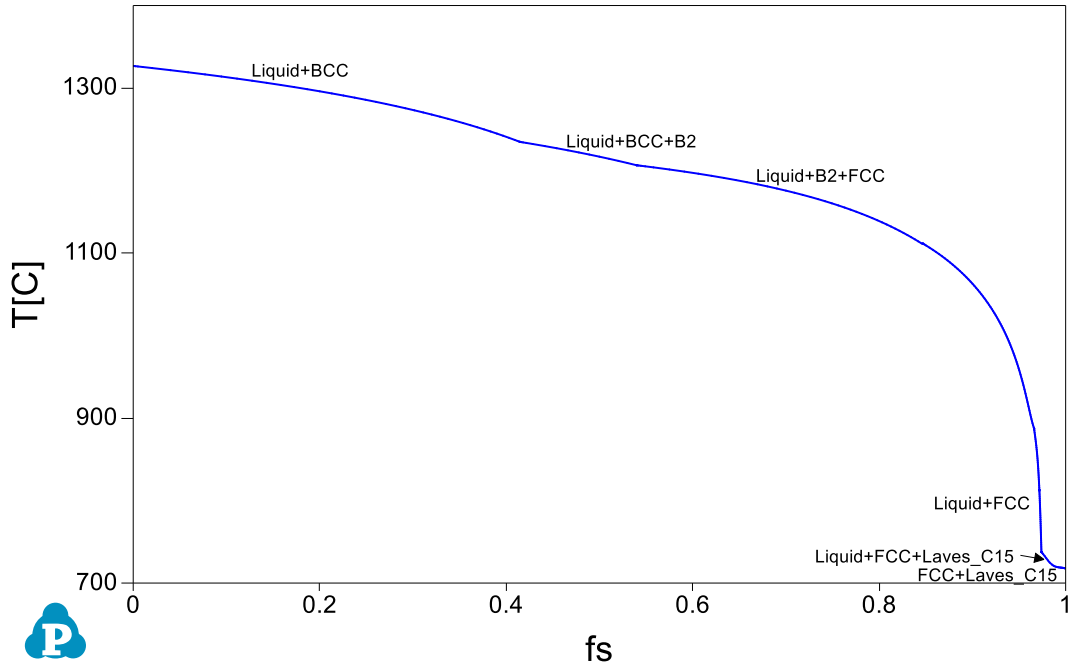

Figure 5.5. Solidification calculation of calculated welding joint with Scheil-Gulliver model by CALPHAD

Table 5.3 The fraction of final possible phases

Fraction of final possible phases (%)			
BCC	B2	FCC	Laves_C15
49.6076	19.5840	29.0128	1.7957

5.4.2 Cracking susceptibility evaluation on the welding joint

Figure 5.6 shows the curve of T vs $(f_S)^{1/2}$ for the nugget composition shown in Table 5.2. The nugget composition has a very high steepness $|dT/d(f_S^{1/2})|$ near $(f_S)^{1/2} = 1$. This can be seen, for instance, in the range of $0.87 < f_S < 0.94$ ($0.933 < (f_S)^{1/2} < 0.970$). The calculated value $|dT/d(f_S^{1/2})| = 2837.8$, near $(f_S)^{1/2} = 1$. This value is much higher than the values of some commercial aluminum alloys such as A206 (1059) and A356 (210) reported in the paper [82]. It means that the nugget composition in this study has higher possibility to have hot cracking. To some extent, it explain why large amount of cracking is observed in Figure 5.3.

5.4.3 Modification of HEA compositions for reducing cracking

Even though it is the first time to observe that HEA can mix Fe and Al alloy together during welding process, hot cracking is still a big issue. In fact, solidification range could be one of the most important factors in hot cracking of dissimilar welding. The hot cracking possibility increases as the solidification range increases, as many studies reported [99-102]. The calculation result shows that the solidification range of the current nugget is larger than 600 °C. To have a better welding joint that with less hot cracking issues, designing HEA composition that could lower the solidification range could be an applicable direction.

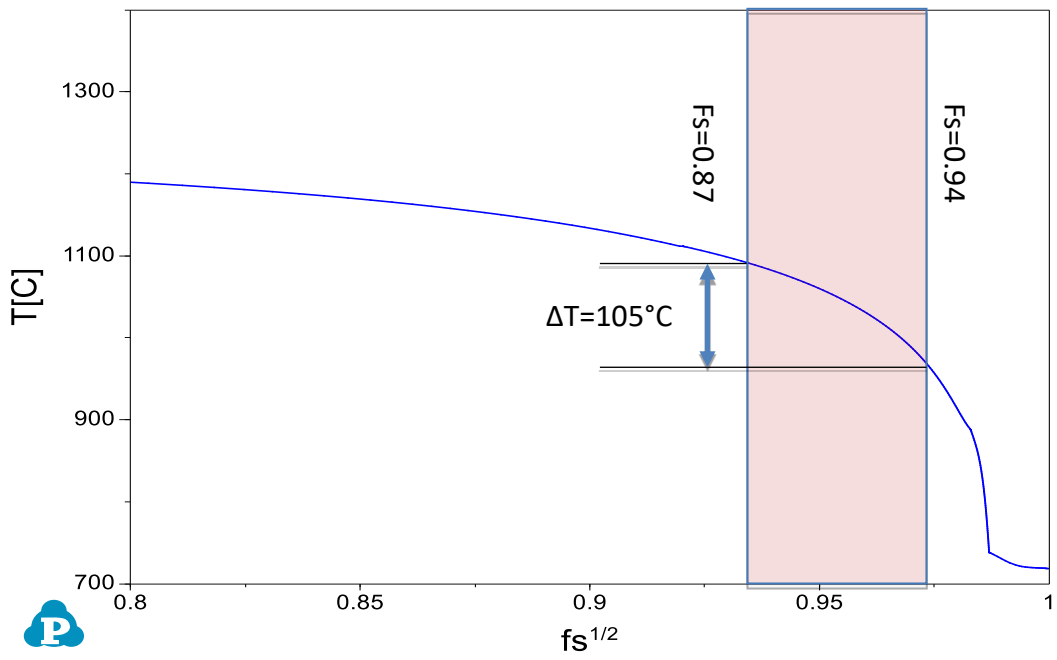

Figure 5.6. Calculated T vs $(f_S)^{1/2}$ of nugget composition

Assuming the dilution of the whole welding joint is 43% HEA + 20.4% Al5754 + 36.6% JAC980. This ratio is estimated from the Table 5.2**Error! Reference source not found.**. Starting from the composition Al2Cu10Fe20Ni30Mn38, the element effect of each element is investigated. Each element will vary from 0 to 35%. The results of Al, Cu, Fe, Ni, Mn effect, are shown in the Table 5.4-5.8.

Two candidate compositions, Al2Cu10Fe20Ni30Mn10 and Al2Cu10Fe20Ni15Mn38, are suggested based on their effect on the nugget's solidification range. The equilibrium analysis both compositions are shown in Figure 5.7. The two candidate compositions are expected to improve the hot cracking issues of the Fe – Al dissimilar welding.

Table 5.4. Calculation of the assuming solidification range and corresponding HEA compositions along with the content of Al change.

HEA compositions					HEA foil			Nugget composition	
Al	Cu	Fe	Ni	Mn	foil liquidus	foil solidus	T(liquidus)	T(solidus)	solidification range
0	10	20	30	38	1,223.96	1,145.30	1323.04	718.2237	604.82
5	10	20	30	38	1,210.44	1,097.30	1327.99	718.4172	609.57
10	10	20	30	38	1,191.06	1,044.29	1331.33	718.7124	612.62
15	10	20	30	38	1,168.92	1,037.91	1333.41	718.992	614.42
20	10	20	30	38	1,145.49	1,030.64	1334.49	719.4686	615.02
25	10	20	30	38	1,184.58	1,021.53	1334.77	720.1007	614.67
30	10	20	30	38	1,240.96	1,009.03	1334.42	720.464	613.96
35	10	20	30	38	1,287.95	990.1635	1333.58	720.7806	612.80

Table 5.5. Calculation of the assuming solidification range and corresponding HEA compositions along with the content of Cu change.

HEA compositions					HEA foil		Nugget composition		
Al	Cu	Fe	Ni	Mn	foil liquidus	foil solidus	T(liquidus)	T(solidus)	solidification range
2	0	20	30	38	1,255.10	1,194.36	1,318.47	506.6478	811.82
2	5	20	30	38	1,235.29	1,155.01	1,321.88	546.1723	775.71
2	10	20	30	38	1,219.62	1,131.10	1,325.24	718.3276	606.91
2	15	20	30	38	1,207.17	1,115.37	1,328.49	719.2926	609.20
2	20	20	30	38	1,197.23	1,104.17	1,331.63	719.9762	611.65
2	25	20	30	38	1,189.28	1,095.64	1,334.63	720.5592	614.07
2	30	20	30	38	1,182.89	1,088.69	1,337.50	720.979	616.52
2	35	20	30	38	1,177.75	1,082.73	1,340.24	721.1171	619.12

Table 5.6. Calculation of the assuming solidification range and corresponding HEA compositions along with the content of Cu change.

HEA compositions					HEA foil		Nugget composition		
Al	Cu	Fe	Ni	Mn	foil liquidus	foil solidus	T(liquidus)	T(solidus)	solidification range
2	10	0	30	38	1,013.56	1,005.34	1,270.14	985.4667	284.67
2	10	5	30	38	1,095.84	1,044.92	1,287.52	1,000.26	287.26
2	10	10	30	38	1,149.96	1,078.30	1,302.05	718.7735	583.28
2	10	15	30	38	1,189.31	1,106.69	1,314.46	718.573	595.89
2	10	20	30	38	1,219.62	1,131.10	1,325.24	718.3276	606.91
2	10	25	30	38	1,243.88	1,152.38	1,334.72	718.0925	616.63
2	10	30	30	38	1,263.85	1,171.15	1,343.17	717.8973	625.27
2	10	35	30	38	1,280.64	1,187.92	1,350.76	717.8372	632.92

Table 5.7. Calculation of the assuming solidification range and corresponding HEA compositions along with the content of Mn change.

HEA compositions					HEA foil		Nugget composition		
Al	Cu	Fe	Ni	Mn	foil liquidus	foil solidus	T(liquidus)	T(solidus)	solidification range
2	10	20	30	0	1,354.78	1,308.96	1,326.46	1,152.76	173.70
2	10	20	30	5	1,323.70	1,264.24	1,330.02	720.7046	609.32
2	10	20	30	10	1,300.05	1,229.67	1,330.99	1,093.31	237.68
2	10	20	30	15	1,280.64	1,202.16	1,330.58	717.2736	613.31
2	10	20	30	20	1,264.03	1,180.13	1,329.56	717.4525	612.11
2	10	20	30	25	1,249.56	1,162.46	1,328.32	717.6673	610.65
2	10	20	30	30	1,236.86	1,148.26	1,327.05	717.955	609.10
2	10	20	30	35	1,225.68	1,136.84	1,325.88	718.2197	607.66

Table 5.8. Calculation of the assuming solidification range and corresponding HEA compositions along with the content of Mn change.

HEA compositions					HEA foil		Nugget composition		
Al	Cu	Fe	Ni	Mn	foil liquidus	foil solidus	T(liquidus)	T(solidus)	solidification range
2	10	20	0	38	1,241.90	978.3408	1,382.64	1,236.73	145.91
2	10	20	5	38	1,236.47	1,081.09	1,369.53	983.6281	385.90
2	10	20	10	38	1,230.77	1,105.31	1,358.44	1,035.15	323.29
2	10	20	15	38	1,225.94	1,114.24	1,348.78	1,028.09	320.69
2	10	20	20	38	1,222.44	1,120.24	1,340.18	719.6055	620.57
2	10	20	25	38	1,220.36	1,125.66	1,332.38	718.8737	613.51
2	10	20	30	38	1,219.62	1,131.10	1,325.24	718.3276	606.91
2	10	20	35	38	1,220.04	1,136.64	1,318.62	717.8223	600.80

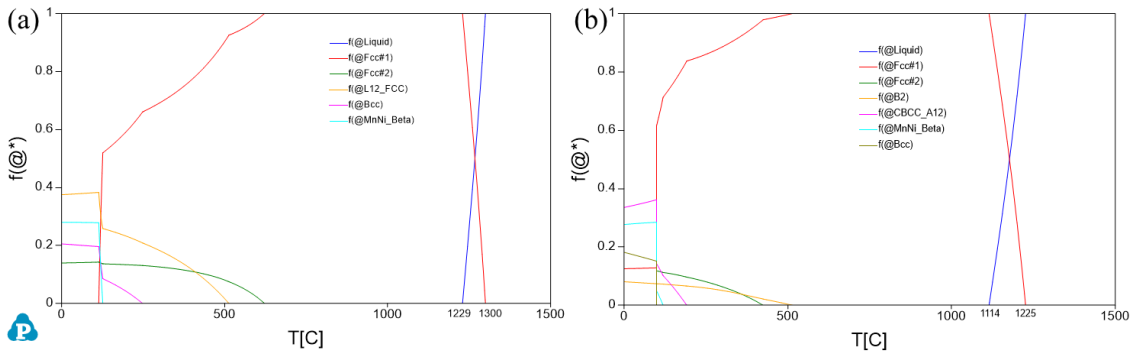

Figure 5.7. Equilibrium solidification analysis of (a) Al2Cu10Fe20Ni30Mn10 and (b) Al2Cu10Fe20Ni15Mn38 by CALPHAD

5.5 Conclusions

In summary, newly design HEA Al2Cu10Fe20Ni30Mn38 is applied in the welding between JAC980 steel and 5754 aluminum alloys. It is the first time to observe three materials mix together and form a welding nugget. The nugget formed a dendritic microstructure with spinodal decomposition. The solidification analysis predicts the nugget is composed by BCC+B2+FCC+Laves phases. The criterion, $|dT/d(f_S^{1/2})|$ near $(f_S)^{1/2} = 1$, is very high for the welding nugget, suggesting that the observed cracking could be highly induced by solidification cracking. New HEA compositions are proposed to reduce the solidification range.

CHAPTER SIX
CONCLUSIONS

In this work, three main tasks have been studied for dissimilar welding between Al alloy and steel with current HEAs, designing HEAs via HTC method, and welding study with newly design HEA.

In the first task, the RSW results show that fusion zone between steel and HEA has formed, while little mixing is observed between the HEA and Al alloys. The failure of joining HEA and Al could be due to the high melting temperature of the HEA. The EDX results show that no diffusion happen between HEA and the Al alloys. The nanoindentation results suggest that intermetallics is formed between Al and the HEA on the Al side, which could worsen the mechanical property of the weld.

In the second task, the phase stability of 35 HEA systems from Al-Cu-X-X-X (X=Co, Cr, Fe, Ni, Mn, Ti, and Zr) is investigated by the high-throughput CALPHAD method. The Al-Cu-Fe-Ni-Mn is found to have the strongest for single FCC phase formation ability among the 35 systems. Further simulation with more data result suggests Al-Cu-Fe-Ni-Mn has 275 FCC single-phase compositions out of 2075 data points. The solidus temperature range of the calculated FCC single-phase compositions are between 1015°C to 1332°C.Suggested candidate composition Al2Cu10Fe20Ni30Mn38 is obtained by the CALPHAD line analysis. This composition is fabricated by arc-melter and heated-treated. The XRD, SEM and EDX results confirmed this composition has FCC single phase structure.

In the third task, newly design HEA Al2Cu10Fe20Ni30Mn38 is applied in the welding between JAC980 steel and 5754 aluminum alloys. It is the first time to observe three materials mix together and form a welding nugget. The nugget formed a dendritic microstructure with spinodal decomposition. The solidification analysis predicts the nugget is composed by BCC+B2+FCC+Laves phases. The criterion, $|dT/d(f_S^{1/2})|$ near $(f_S)^{1/2} = 1$, is very high for the welding nugget, suggesting that the observed cracking could be highly induced by solidification cracking. New HEA compositions are proposed to reduce the solidification range.

REFERENCES

[1] H. Huh, W. Kang, Electrothermal analysis of electric resistance spot welding processes by a 3-D finite element method, Journal of Materials Processing Technology 63(1-3) (1997) 672-677.

[2] J.W. Yeh, S.K. Chen, S.J. Lin, J.Y. Gan, T.S. Chin, T.T. Shun, C.H. Tsau, S.Y. Chang, Nanostructured high-entropy alloys with multiple principal elements: novel alloy design concepts and outcomes, Advanced Engineering Materials 6(5) (2004) 299-303.

[3] Y. Zhang, T.T. Zuo, Z. Tang, M.C. Gao, K.A. Dahmen, P.K. Liaw, Z.P. Lu, Microstructures and properties of high-entropy alloys, Progress in Materials Science 61 (2014) 1-93.

[4] Z. Tang, M.C. Gao, H. Diao, T. Yang, J. Liu, T. Zuo, Y. Zhang, Z. Lu, Y. Cheng, Y. Zhang, Aluminum alloying effects on lattice types, microstructures, and mechanical behavior of high-entropy alloys systems, Jom 65(12) (2013) 1848-1858.

[5] Y. Zhang, Z. Lu, S. Ma, P. Liaw, Z. Tang, Y. Cheng, M. Gao, Guidelines in predicting phase formation of high-entropy alloys, Mrs Communications 4(2) (2014) 57.

[6] M. Lucas, G. Wilks, L. Mauger, J.A. Munoz, O. Senkov, E. Michel, J. Horwath, S. Semiatin, M.B. Stone, D.L. Abernathy, Absence of long-range chemical ordering in equimolar FeCoCrNi, Applied Physics Letters 100(25) (2012) 251907.

[7] Y. Zhang, Y.J. Zhou, J.P. Lin, G.L. Chen, P.K. Liaw, Solid-solution phase formation rules for multi-component alloys, Advanced Engineering Materials 10(6) (2008) 534-538.

[8] L.J. Santodonato, Y. Zhang, M. Feygenson, C.M. Parish, M.C. Gao, R.J. Weber, J.C. Neuefeind, Z. Tang, P.K. Liaw, Deviation from high-entropy configurations in the atomic distributions of a multi-principal-element alloy, Nature communications 6 (2015).

[9] Y. Lu, Y. Dong, S. Guo, L. Jiang, H. Kang, T. Wang, B. Wen, Z. Wang, J. Jie, Z. Cao, A promising new class of high-temperature alloys: eutectic high-entropy alloys, Scientific reports 4 (2014).

[10] M.A. Hemphill, T. Yuan, G. Wang, J. Yeh, C. Tsai, A. Chuang, P. Liaw, Fatigue behavior of Al 0.5 CoCrCuFeNi high entropy alloys, Acta Materialia 60(16) (2012) 5723-5734.

[11] B. Gludovatz, A. Hohenwarter, D. Catoor, E.H. Chang, E.P. George, R.O. Ritchie, A fracture-resistant high-entropy alloy for cryogenic applications, Science 345(6201) (2014) 1153-1158.

[12] A. Takeuchi, K. Amiya, T. Wada, K. Yubuta, W. Zhang, High-entropy alloys with a hexagonal close-packed structure designed by equi-atomic alloy strategy and binary phase diagrams, Jom 66(10) (2014) 1984-1992.

[13] A. Takeuchi, K. Amiya, T. Wada, K. Yubuta, Alloy design for high-entropy alloys based on Pettifor map for binary compounds with 1: 1 stoichiometry, Intermetallics 66 (2015) 56-66.

[14] Z. Tang, T. Yuan, C.-W. Tsai, J.-W. Yeh, C.D. Lundin, P.K. Liaw, Fatigue behavior of a wrought Al 0.5 CoCrCuFeNi two-phase high-entropy alloy, Acta Materialia 99 (2015) 247-258.

[15] Y. Shi, B. Yang, P.K. Liaw, Corrosion-Resistant High-Entropy Alloys: A Review, Metals 7(2) (2017) 43.

[16] Y. Shi, B. Yang, X. Xie, J. Brechtl, K.A. Dahmen, P.K. Liaw, Corrosion of Al xCoCrFeNi high-entropy alloys: Al-content and potential scan-rate dependent pitting behavior, Corrosion Science (2017).

[17] N. Shah, M. Rahul, S. Bysakh, G. Phanikumar, Microstructure stability during high temperature deformation of FeCoNiCrTa eutectic high entropy alloy through nano-scale precipitation, Materials Science and Engineering: A (2021) 141793.

[18] K.-M. Hsu, S.-H. Chen, C.-S. Lin, Microstructure and corrosion behavior of FeCrNiCoMnx (x= 1.0, 0.6, 0.3, 0) high entropy alloys in 0.5 M H2SO4, Corrosion Science (2021) 109694.

[19] L. Kaufman, H. Bernstein, Computer calculation of phase diagrams. With special reference to refractory metals, (1970).

[20] N. Saunders, A.P. Miodownik, CALPHAD (calculation of phase diagrams): a comprehensive guide, Elsevier1998.

[21] Y.M. Muggianu, M. Gambino, J. Bros, Enthalpies of formation of liquid alloys bismuth-gallium-tin at 723k-choice of an analytical representation of integral and partial thermodynamic functions of mixing for this ternary-system, Journal de Chimie Physique et de Physico-Chimie Biologique 72(1) (1975) 83-88.

[22] I. Ansara, Comparison of methods for thermodynamic calculation of phase diagrams, International Metals Reviews 24(1) (1979) 20-53.

[23] Y.A. Chang, S. Chen, F. Zhang, X. Yan, F. Xie, R. Schmid-Fetzer, W.A. Oates, Phase diagram calculation: past, present and future, Progress in Materials Science 49(3) (2004) 313-345.

[24] U.R. Kattner, The thermodynamic modeling of multicomponent phase equilibria, JOM 49(12) (1997) 14-19.

[25] X.-W. Qiu, C.-G. Liu, Microstructure and properties of Al2CrFeCoCuTiNix high-entropy alloys prepared by laser cladding, Journal of Alloys and Compounds 553 (2013) 216-220.

[26] I. Voiculescu, V. Geanta, I. Vasile, R. Stefanoiu, M. Tonoiu, Characterisation of weld deposits using as filler metal a high entropy alloy, Journal of Optoelectronics and Advanced Materials 15(7-8) (2013) 650-654.

[27] M. Komarasamy, N. Kumar, Z. Tang, R. Mishra, P. Liaw, Effect of microstructure on the deformation mechanism of friction stir-processed Al0. 1CoCrFeNi high entropy alloy, Materials Research Letters 3(1) (2015) 30-34.

[28] Z. Wu, S.A. David, Z. Feng, H. Bei, Weldability of a high entropy CrMnFeCoNi alloy, Scripta Materialia 124 (2016) 81-85.

[29] Z. Zhu, Y. Sun, M. Goh, F. Ng, Q. Nguyen, H. Fujii, S. Nai, J. Wei, C. Shek, Friction stir welding of a CoCrFeNiAl0. 3 high entropy alloy, Materials Letters 205 (2017) 142-144.

[30] H. Nam, C. Park, C. Kim, H. Kim, N. Kang, Effect of post weld heat treatment on weldability of high entropy alloy welds, Science and Technology of Welding and Joining 23(5) (2018) 420-427.

[31] S. Park, C. Park, Y. Na, H.-S. Kim, N. Kang, Effects of (W, Cr) carbide on grain refinement and mechanical properties for CoCrFeMnNi high entropy alloys, Journal of Alloys and Compounds (2018).

[32] R. Sokkalingam, K. Sivaprasad, V. Muthupandi, M. Duraiselvam, Characterization of Laser Beam Welded Al0. 5CoCrFeNi High-Entropy Alloy, Key Engineering Materials, Trans Tech Publ, 2018, pp. 448-453.

[33] Z. Zhu, Y. Sun, F. Ng, M. Goh, P. Liaw, H. Fujii, Q. Nguyen, Y. Xu, C. Shek, S. Nai, Friction-stir welding of a ductile high entropy alloy: microstructural evolution and weld strength, Materials Science and Engineering: A 711 (2018) 524-532.

[34] C. Chen, R. Kovacevic, Joining of Al 6061 alloy to AISI 1018 steel by combined effects of fusion and solid state welding, International Journal of Machine Tools and Manufacture 44(11) (2004) 1205-1214.

[35] R. Qiu, C. Iwamoto, S. Satonaka, Interfacial microstructure and strength of steel/aluminum alloy joints welded by resistance spot welding with cover plate, Journal of Materials Processing Technology 209(8) (2009) 4186-4193.

[36] R. Qiu, S. Satonaka, C. Iwamoto, Effect of interfacial reaction layer continuity on the tensile strength of resistance spot welded joints between aluminum alloy and steels, Materials & Design 30(9) (2009) 3686-3689.

[37] X. Sun, E.V. Stephens, M.A. Khaleel, H. Shao, M. Kimchi, Resistance spot welding of aluminum alloy to steel with transition material-from process to performance-part I: experimental study, WELDING JOURNAL-NEW YORK- 83 (2004) 188-S.

[38] E. Taban, J.E. Gould, J.C. Lippold, Dissimilar friction welding of 6061-T6 aluminum and AISI 1018 steel: Properties and microstructural characterization, Materials & design 31(5) (2010) 2305-2311.

[39] M. Torkamany, S. Tahamtan, J. Sabbaghzadeh, Dissimilar welding of carbon steel to 5754 aluminum alloy by Nd: YAG pulsed laser, Materials & Design 31(1) (2010) 458-465.

[40] L. Tricarico, R. Spina, D. Sorgente, M. Brandizzi, Effects of heat treatments on mechanical properties of Fe/Al explosion-welded structural transition joints, Materials & Design 30(7) (2009) 2693-2700.

[41] S. Yang, J. Zhang, J. Lian, Y. Lei, Welding of aluminum alloy to zinc coated steel by cold metal transfer, Materials & Design 49 (2013) 602-612.

[42] H. Zhang, J. Feng, P. He, B. Zhang, J. Chen, L. Wang, The arc characteristics and metal transfer behaviour of cold metal transfer and its use in joining aluminium to zinc-coated steel, Materials Science and Engineering: A 499(1) (2009) 111-113.

[43] S. Satonaka, C. Iwamoto, R. Qui, T. Fujioka, Trends and new applications of spot welding for aluminium alloy sheets, Welding international 20(11) (2006) 858-864.

[44] W.C. Oliver, G.M. Pharr, AN IMPROVED TECHNIQUE FOR DETERMINING HARDNESS AND ELASTIC-MODULUS USING LOAD AND DISPLACEMENT SENSING INDENTATION EXPERIMENTS, Journal of Materials Research 7(6) (1992) 1564-1583.

[45] W.C. Oliver, G.M. Pharr, Measurement of hardness and elastic modulus by instrumented indentation: Advances in understanding and refinements to methodology, Journal of Materials Research 19(1) (2004) 3-20.

[46] W.D. Nix, H. Gao, Indentation size effects in crystalline materials: a law for strain gradient plasticity, J. Mech. Phys. Solics 46(3) (1998) 411-425.

[47] Y. Huang, F. Zhang, K.C. Hwang, W.D. Nix, G.M. Pharr, G. Feng, A model of size effects in nano-indentation, J. Mech. Phys. Solids 54(8) (2006) 1668-1686.

[48] B. Cantor, I. Chang, P. Knight, A. Vincent, Microstructural development in equiatomic multicomponent alloys, Materials Science and Engineering: A 375 (2004) 213-218.

[49] M.C. Gao, J.-W. Yeh, P.K. Liaw, Y. Zhang, High-entropy alloys: fundamentals and applications, Springer2016.

[50] O. Senkov, J. Miller, D. Miracle, C. Woodward, Accelerated exploration of multi-principal element alloys with solid solution phases, Nature communications 6 (2015) 6529.

[51] O. Senkov, G. Wilks, D. Miracle, C. Chuang, P. Liaw, Refractory high-entropy alloys, Intermetallics 18(9) (2010) 1758-1765.

[52] C. Lee, G. Song, M.C. Gao, R. Feng, P. Chen, J. Brechtl, Y. Chen, K. An, W. Guo, J.D. Poplawsky, Lattice distortion in a strong and ductile refractory high-entropy alloy, Acta Materialia 160 (2018) 158-172.

[53] P. Chen, C. Lee, S.-Y. Wang, M. Seifi, J.J. Lewandowski, K.A. Dahmen, H. Jia, X. Xie, B. Chen, J.-W. Yeh, C.-W. Tsai, T. Yuan, P.K. Liaw, Fatigue behavior of high-entropy alloys: A review, Science China Technological Sciences 61(2) (2018) 168-178.

[54] W.D. Li, S.Y. Chen, P.K. Liaw, Discovery and design of fatigue-resistant high-entropy alloys, Scripta Materialia 187 (2020) 68-75.

[55] K.V.S. Thurston, B. Gludovatz, Q. Yu, G. Laplanche, E.P. George, R.O. Ritchie, Temperature and load-ratio dependent fatigue-crack growth in the CrMnFeCoNi high-entropy alloy, Journal of Alloys and Compounds 794 (2019) 525-533.

[56] K.V.S. Thurston, B. Gludovatz, A. Hohenwarter, G. Laplanche, E.P. George, R.O. Ritchie, Effect of temperature on the fatigue-crack growth behavior of the high-entropy alloy CrMnFeCoNi, Intermetallics 88 (2017) 65-72.

[57] L. Zhang, P. Yu, H. Cheng, H. Zhang, H. Diao, Y. Shi, B. Chen, P. Chen, R. Feng, J. Bai, Q. Jing, M. Ma, P.K. Liaw, G. Li, R. Liu, Nanoindentation Creep Behavior of an Al0.3CoCrFeNi High-Entropy Alloy, Metallurgical and Materials Transactions A 47(12) (2016) 5871-5875.

[58] J. Rao, H. Diao, V. Ocelík, D. Vainchtein, C. Zhang, C. Kuo, Z. Tang, W. Guo, J. Poplawsky, Y. Zhou, Secondary phases in AlxCoCrFeNi high-entropy alloys: An in-situ TEM heating study and thermodynamic appraisal, Acta Materialia 131 (2017) 206-220.

[59] M.C. Troparevsky, J.R. Morris, P.R. Kent, A.R. Lupini, G.M. Stocks, Criteria for predicting the formation of single-phase high-entropy alloys, Physical Review X 5(1) (2015) 011041.

[60] X. Liu, G. Sha, Q. Wu, Y. Liang, J. Huang, K. Jin, Y. Xue, B. Wang, L. Wang, L. Wang, Phase stability of an high-entropy Al-Cr-Fe-Ni-V alloy with exceptional mechanical properties: First-principles and APT investigations, Computational Materials Science 170 (2019) 109161.

[61] Z. Li, F. Körmann, B. Grabowski, J. Neugebauer, D. Raabe, Ab initio assisted design of quinary dual-phase high-entropy alloys with transformation-induced plasticity, Acta Materialia 136 (2017) 262-270.

[62] W. Li, J. Tang, Q. Wang, H. Fan, Molecular Dynamics Simulations on the Mechanical Behavior of AlCoCrCu 0.5 FeNi High-Entropy Alloy Nanopillars, TMS 2019 148th Annual Meeting & Exhibition Supplemental Proceedings, Springer, 2019, pp. 1271-1280.

[63] A. Korchuganov, I. Lutsenko, Molecular dynamics research of mechanical, diffusion and thermal properties of CoCrFeMnNi high-entropy alloys, AIP Conference Proceedings, AIP Publishing, 2018, p. 040046.

[64] R. Feng, M.C. Gao, C. Lee, M. Mathes, T. Zuo, S. Chen, J.A. Hawk, Y. Zhang, P.K. Liaw, Design of light-weight high-entropy alloys, Entropy 18(9) (2016) 333.

[65] M. Zheng, W. Ding, W. Cao, S. Hu, Q. Huang, A quick screening approach for design of multi-principal element alloy with solid solution phase, Materials & Design 179 (2019) 107882.

[66] F. Tancret, I. Toda-Caraballo, E. Menou, P.E.J.R. Díaz-Del, Designing high entropy alloys employing thermodynamics and Gaussian process statistical analysis, Materials & Design 115 (2017) 486-497.

[67] O. Senkov, J. Miller, D. Miracle, C. Woodward, Accelerated exploration of multi-principal element alloys for structural applications, Calphad 50 (2015) 32-48.

[68] C. Zhang, M.C. Gao, CALPHAD modeling of high-entropy alloys, High-Entropy Alloys, Springer2016, pp. 399-444.

[69] F. Zhang, C. Zhang, S.-L. Chen, J. Zhu, W.-S. Cao, U.R. Kattner, An understanding of high entropy alloys from phase diagram calculations, Calphad 45 (2014) 1-10.

[70] C. Zhang, F. Zhang, H. Diao, M.C. Gao, Z. Tang, J.D. Poplawsky, P.K. Liaw, Understanding phase stability of Al-Co-Cr-Fe-Ni high entropy alloys, Materials & Design 109 (2016) 425-433.

[71] C. Ng, S. Guo, J. Luan, Q. Wang, J. Lu, S. Shi, C. Liu, Phase stability and tensile properties of Co-free Al0. 5CrCuFeNi2 high-entropy alloys, Journal of alloys and compounds 584 (2014) 530-537.

[72] U.R. Kattner, The CALPHAD method and its role in material and process development, Tecnologia em metalurgia, materiais e mineracao 13(1) (2016) 3.

[73] W.-M. Choi, S. Jung, Y.H. Jo, S. Lee, B.-J. Lee, Design of new face-centered cubic high entropy alloys by thermodynamic calculation, Metals and Materials International 23(5) (2017) 839-847.

[74] S.-L. Chen, S. Daniel, F. Zhang, Y. Chang, X.-Y. Yan, F.-Y. Xie, R. Schmid-Fetzer, W. Oates, The PANDAT software package and its applications, Calphad 26(2) (2002) 175-188.

[75] W. Cao, S.-L. Chen, F. Zhang, K. Wu, Y. Yang, Y. Chang, R. Schmid-Fetzer, W. Oates, PANDAT software with PanEngine, PanOptimizer and PanPrecipitation for multi-component phase diagram calculation and materials property simulation, Calphad 33(2) (2009) 328-342.

[76] S.-L. Chen, F. Zhang, F.-Y. Xie, S. Daniel, X.-Y. Yan, Y. Chang, R. Schmid-Fetzer, W. Oates, Calculating phase diagrams using PANDAT and PanEngine, Jom 55(12) (2003) 48-51.

[77] C. Li, J.C. Li, M. Zhao, Q. Jiang, Effect of alloying elements on microstructure and properties of multiprincipal elements high-entropy alloys, Journal of Alloys and Compounds 475(1) (2009) 752-757.

[78] J. Chen, P. Niu, Y. Liu, Y. Lu, X. Wang, Y. Peng, J. Liu, Effect of Zr content on microstructure and mechanical properties of AlCoCrFeNi high entropy alloy, Materials & Design 94 (2016) 39-44.

[79] N.Y. Yurchenko, N.D. Stepanov, A.O. Gridneva, M.V. Mishunin, G.A. Salishchev, S.V. Zherebtsov, Effect of Cr and Zr on phase stability of refractory Al-Cr-Nb-Ti-V-Zr high-entropy alloys, Journal of Alloys and Compounds 757 (2018) 403-414.

[80] G. Gulliver, The quantitative effect of rapid cooling upon the constitution of binary alloys, J. Inst. Met 9(1) (1913) 120-157.

[81] E. Scheil, Bemerkungen zur schichtkristallbildung, Zeitschrift für Metallkunde 34(3) (1942) 70-72.

[82] S. Kou, A criterion for cracking during solidification, Acta Materialia 88 (2015) 366-374.

[83] S. Kou, Solidification and liquation cracking issues in welding, Jom 55(6) (2003) 37-42.

[84] S. Kou, Solidification cracking susceptibility associated with a teardrop-shaped weld pool, Science and Technology of Welding and Joining 26(4) (2021) 341-347.

[85] J. Liu, P. Zeng, S. Kou, Solidification cracking susceptibility of quaternary aluminium alloys, Science and Technology of Welding and Joining 26(3) (2021) 244-257.

[86] C. Xia, S. Kou, Calculating the susceptibility of carbon steels to solidification cracking during welding, Metallurgical and Materials Transactions B 52(1) (2021) 460-469.

[87] K. Liu, P. YU, S. KOU, Solidification Cracking Susceptibility of Stainless Steels: New Test and Explanation, Welding Journal 99(10) (2020).

[88] C. Xia, S. Kou, Evaluating susceptibility of carbon steels to solidification cracking by transverse-motion weldability test, Science and Technology of Welding and Joining 25(8) (2020) 706-711.

[89] C. Xia, S. Kou, Evaluating susceptibility of Ni-base alloys to solidification cracking by transverse-motion weldability test, Science and Technology of Welding and Joining 25(8) (2020) 690-697.

[90] T. Soysal, S. Kou, A simple test for assessing solidification cracking susceptibility and checking validity of susceptibility prediction, Acta Materialia 143 (2018) 181-197.

[91] K. Liu, S. Kou, Susceptibility of magnesium alloys to solidification cracking, Science and Technology of Welding and Joining 25(3) (2020) 251-257.

[92] J. Liu, S. Kou, Susceptibility of ternary aluminum alloys to cracking during solidification, Acta Materialia 125 (2017) 513-523.

[93] T. Soysal, S. Kou, Predicting effect of filler metals on solidification cracking susceptibility of 2024 Al and 6061 Al, Science and Technology of Welding and Joining 24(6) (2019) 559-565.

[94] J. Liu, H.P. Duarte, S. Kou, Evidence of back diffusion reducing cracking during solidification, Acta Materialia 122 (2017) 47-59.

[95] J. Liu, S. Kou, Predicting Susceptibility of Binary Mg Alloys to Cracking During Solidification, Available at SSRN 3301216 (2018).

[96] Y.-F. Kao, T.-J. Chen, S.-K. Chen, J.-W. Yeh, Microstructure and mechanical property of as-cast,-homogenized, and-deformed AlxCoCrFeNi ($0 \leq x \leq 2$) high-entropy alloys, Journal of Alloys and Compounds 488(1) (2009) 57-64.

[97] C. Li, M. Zhao, J. Li, Q. Jiang, B 2 structure of high-entropy alloys with addition of Al, Journal of Applied Physics 104(11) (2008) 113504.

[98] H.-P. Chou, Y.-S. Chang, S.-K. Chen, J.-W. Yeh, Microstructure, thermophysical and electrical properties in AlxCoCrFeNi ($0 \leq x \leq 2$) high-entropy alloys, Materials Science and Engineering: B 163(3) (2009) 184-189.

[99] A. Pozdniakov, V. Zolotorevskiy, Determining hot cracking index of Al–Si–Cu–Mg casting alloys calculated using effective solidification range, International Journal of Cast Metals Research 27(4) (2014) 193-198.

[100] J. Lippold, W. Savage, Solidification of austenitic stainless steel weldments: Part III--the effect of solidification behavior on hot cracking susceptibility, WELDING J. 61(12) (1982) 388.

[101] L. Katgerman, D. Eskin, In search of the prediction of hot cracking in aluminium alloys, Hot cracking phenomena in welds II, Springer2008, pp. 11-26.

[102] I. Novikov, O. Grushko, Hot cracking susceptibility of Al–Cu–Li and Al–Cu–Li–Mn alloys, Materials Science and technology 11(9) (1995) 926-932.

VITA

Peiyong Chen was born in Guangdong, China. He graduated with a B.S. degree from the Department of Materials Science and Engineering, Xi'an Jiaotong University in 2014. Later he started to work as a graduate research assistant in the University of Tennessee, Knoxville in 2014. He obtained a M.S. degree from the Department of Materials Science and Engineering in 2017. In December 2021, he graduated from the University of Tennessee with Doctor of Philosophy degree in Materials Science and Engineering (concentrated in Metallurgy).